

Towards Customized Knowledge Distillation for Chip-Level Dense Image Predictions

Dong Zhang, Pingcheng Dong, Long Chen, Kwang-Ting Cheng, *Fellow, IEEE*

Abstract—It has been revealed that efficient dense image prediction (EDIP) models designed for AI chips, trained using the knowledge distillation (KD) framework, encounter two key challenges, including *maintaining boundary region completeness* and *ensuring target region connectivity*, despite their favorable real-time capacity to recognize the main object regions. In this work, we propose a customized boundary and context knowledge distillation (BCKD) method for EDIPs, which facilitates the targeted KD from large accurate teacher models to compact small student models. Specifically, the *boundary distillation* focuses on extracting explicit object-level boundaries from the hierarchical feature maps to enhance the student model’s mask quality in boundary regions. Meanwhile, the *context distillation* leverages self-relations as a bridge to transfer implicit pixel-level contexts from the teacher model to the student model, ensuring strong connectivity in target regions. Our proposed method is specifically designed for the EDIP tasks and is characterized by its simplicity and efficiency. Theoretical analysis and extensive experimental results across semantic segmentation, object detection, and instance segmentation on five representative datasets demonstrate the effectiveness of BCKD, resulting in well-defined object boundaries and smooth connecting regions.

Index Terms—Model compression, Knowledge distillation, Dense image predictions, Boundary and context learning.

I. INTRODUCTION

THE dense image prediction (DIP) tasks, *e.g.*, semantic segmentation [1], object detection [2], and instance segmentation [3], are fundamental yet challenging research problems within both domains of computer vision and multimedia computing [4], [5]. The objective of these tasks is to assign a semantic label to each object and/or pixel of the given image [4]. In recent years, advancements in general-purpose GPU technology have resulted in notable enhancements in both size and accuracy of sophisticated DIP models [6], [7], *e.g.*, Mask2Former [8], SegNeXt [9], and SAM [10]. However, deploying large and accurate DIP models on resource-constrained edge computing devices, *e.g.*, artificial intelligence chips [11], presents significant challenges due to the substantial computational costs and high memory consumptions associated with these models [3].

Compressing large DIP models into compact efficient DIP (EDIP) models offers an intuitive and cost-effective solution to address the severe resource limitations associated with mapping vision models onto edge computing devices [13], [14]. In particular, the cross-architecture manner enables compressed

models to seamlessly adapt to customized edge devices, eliminating the need for hardware modifications while maintaining computational efficiency. This manner significantly reduces deployment complexity and enhances the flexibility of model inference across heterogeneous edge computing platforms [15]. To achieve this goal and develop accuracy-preserving EDIP models, knowledge distillation (KD) [16], [17], a prevalent model compression technology, has been pragmatically employed by using a small efficient model (*i.e.*, the student model) by imitating the behavior of a large accurate model (*i.e.*, the teacher model) in training [16], [18]. During inference, only the student model is utilized, allowing for a highly-efficient recognition pattern while simultaneously reducing the model size [13], [14], [19]. Despite significant advancements by current KD methods across multiple dimensions, including sophisticated distillation strategies [19] and complex distillation content [20], the inherent complexity of DIP continues to pose two critical challenges for existing approaches, particularly for the efficient compact models. The details are as follows:

Primary KD methods mainly emphasize the imitation of general knowledge (*e.g.*, features, regions, and logits) while overlooking the nuanced understanding of features along objective semantic boundaries and connecting internal regions essential for EDIPs [14], [21]. Particularly, since the small student model often predicts the main object regions fairly well but fails in boundary and connecting regions [6], [22], [23], the conventional utilization of task-agnostic general KD may not be effective enough and can be considered purposeless and redundant [18], [24], [25], remaining a performance gap between the obtained results and the expected ones [26]. For instance, we recommend the representative semantic segmentation task as an example. As shown in Figure 1, the small student model (*i.e.*, PSPNet-18 [27]) in (c) produces inferior results compared to the large teacher model (*i.e.*, PSPNet-101 [27]) results in (b). The student model wrongly segments the boundary regions of “*curtain*” and “*door*” as the background category or other foreground objects, and produces fragmented “*bed valance*” and “*chair*”, breaking the regional relation connectivity. Generally, the common errors observed in the outputs of the small student model can be summarized as *maintaining boundary region completeness* and *ensuring target region connectivity*.

To mitigate these errors and narrow the performance gap, in this paper, we propose a customized and targeted KD strategy termed as **Boundary and Context Knowledge Distillation (BCKD)**. By “customized”, we mean that our method’s inherent ability to synergistically address the common errors

D. Zhang, P. Dong, and K.-T. Cheng are with the Department of Electronic and Computer Engineering, HKUST, Hong Kong, China. E-mail: {dongz, tim-cheng}@ust.hk, pingcheng.dong@connect.ust.hk.

L. Chen is with the Department of Computer Science and Engineering, HKUST, Hong Kong, China. E-mail: longchen@ust.hk.

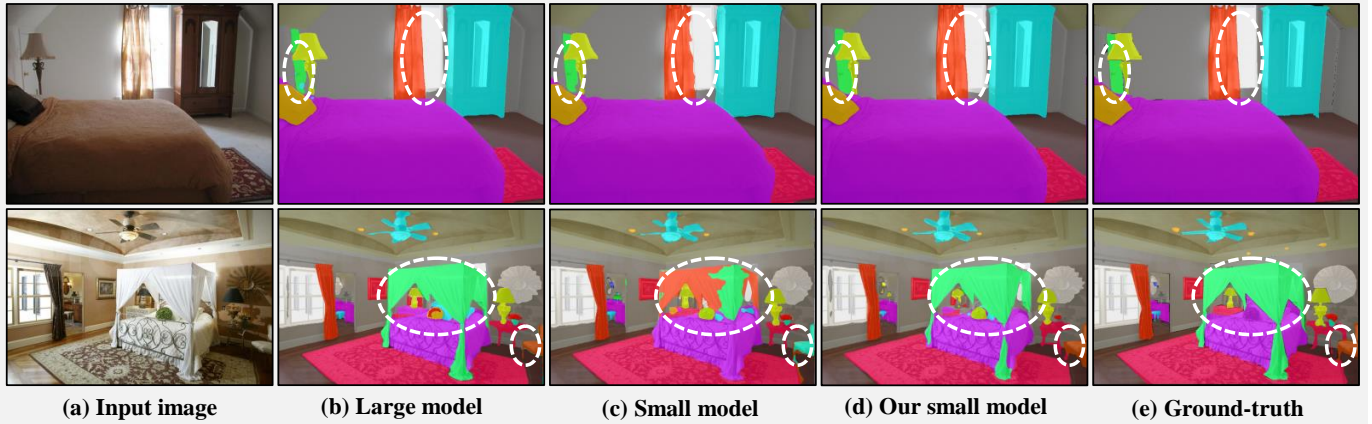


Figure 1. Two representative cases that small models are prone to produce errors. Result comparisons between large accurate models (b) and small efficient models (c) show that the latter tend to make errors in *maintaining boundary region completeness* (e.g., the “curtain” and the “door”) and *preserving target region connectivity* (e.g., the “bed valance” and the “chair”). With the help of our BCKD in (d), small models can address the two types of errors, leading to crisp region boundaries and smooth connecting regions. “w/” denotes with the corresponding implementation. Samples are from the ADE20K dataset [12].

present in existing EDIP models, while also coexisting with other methods (ref. Sec. V-C). BCKD mainly consists of two key components: the *boundary distillation* and the *context distillation*, aimed at rectifying the typical common errors encountered by EDIP models in *maintaining boundary region completeness* and *ensuring target region connectivity*, respectively. Specifically, *boundary distillation* involves generating explicit object-level boundaries from the hierarchical backbone features, enhancing the completeness of the student model’s masks in boundary regions (ref. Sec. IV-B). At the same time, *context distillation* transfers implicit pixel-level contexts from the teacher model to the student model through self-relations, ensuring robust connectivity in the student’s masks (ref. Sec. IV-C). BCKD is tailored specifically for EDIP tasks and offers a more targeted distillation pattern and a more tailored distillation manner compared to conventional task-agnostic KD methods. From a rigorous theoretical perspective, we establish and prove the effectiveness of our BCKD method (ref. Sec. IV-E). To validate the superior accuracy, we conducted extensive experiments in three representative dense image prediction tasks, including semantic segmentation, object detection, and instance segmentation, utilizing five challenging datasets such as Pascal VOC 2012 [28], Cityscapes [29], ADE20K [12], COCO-Stuff 10K [30], and MS-COCO 2017 [31]. Qualitatively, BCKD produces sharp region boundaries and smooth connecting regions, addressing challenges that have hindered EDIP models. Quantitatively, BCKD consistently improves the accuracy of baseline models in various metrics, achieving competitive performance.

The main contributions are summarized as the following three folds: **1)** We revealed two prevalent issues in existing EDIP models: maintaining boundary region completeness and ensuring target region connectivity. **2)** We proposed a customized and targeted boundary and context knowledge distillation method. Our method not only demonstrates inherent coherence, but also possesses the capability to coexist with other methods. **3)** Theoretical analysis demonstrates the superior effectiveness of our BCKD. **4)** Experimental evaluations across various tasks, baselines and datasets illustrate the superior accuracy of our method in comparison with existing methods.

II. RELATED WORK

A. Dense Image Prediction (DIP) Tasks

DIP is a fundamental research problem within the fields of computer vision and multimedia computing, with the objective of assigning each object and/or pixel in an input image to a predefined category label, thereby enabling comprehensive semantic image recognition [1], [4], [32], [33]. Current mainstream DIP models can be roughly classified into the following three categories based on their backbone components: 1) methods based on CNNs [1], [34]–[36], 2) methods based on ViT¹ [7], [39], [40], and 3) methods that combine CNNs and ViT [41], [42]. The key difference between these types of architectures is the approach used for feature extraction and how the extracted features are utilized in enhancing the capacity of CNNs models to capture contextual features [6], [43], increasing the capacity of ViT models to capture local features [42], [44], [45], and leveraging low-level features to improve representation capacity [46], [47] for achieving favorable results.

Concretely, due to differences in feature extraction manners between CNNs and ViT, these two categories exhibit slight performance differences [39]–[42]. For example, CNNs methods are better at predicting local object regions, while ViT methods, due to their stronger contextual information, can produce more complete object masks. Fortunately, the mixture of CNNs and ViT (e.g., CMT [48], CvT [44], ConFormer [42], CAE-Great [46], and visual Mamba [37]) uses the representation strengths of both patterns, resulting in highly satisfactory recognition performance [49]–[51]. In addition to these fundamental categories, there are advanced approaches that also utilize task-specific training tricks (e.g., graph reasoning [45], linear attention [52], multi-scale representation [53]) to improve the accuracy. However, while current methods have achieved promising accuracy, mapping these models on resource constrained edge computing devices remains challeng-

¹We consider the visual state space model-based methods as a specialized Transformer architecture [37], [38], owing to its structural similarities with the ViT model. Besides, we do not address the content related to these models. Therefore, we will no longer have separate discussions on this aspect.

ing because these devices typically have limited computation resources and memory consumptions [11], [54]. In this work, we do not intend to modify the network architecture. We first investigate the result disparities between small and large models and then propose a novel KD strategy tailored to the EDIP models. We aim at improving the recognition accuracy of small models without requiring any extra training data or increasing the inference costs.

B. Knowledge Distillation (KD) in DIPs

KD is a well-established model compression technology that aims to transfer valuable knowledge from a large accuracy teacher model to a small efficient student model, with the objective of enhancing the student's accuracy during inference [20], [55], [56]. It is worth mentioning that the effectiveness of KD in cross-architecture scenarios has enabled significant flexibility in artificial intelligence chip design, as it eliminates the need to modify the underlying operators while maintaining model performance, which provides a practical solution for hardware adaptation without compromising computational efficiency [11]. The key factors for the success of KD in DIPs are: 1) the types of knowledge being distilled, *e.g.*, general knowledge: features and logits, and task-specific knowledge: class edge for semantic segmentation and object localization for object detection, 2) the distillation strategies employed, *e.g.*, offline distillation [57], online distillation [58], and self-distillation [59], and 3) the architecture of the teacher-student pair, *e.g.*, multi-teacher KD [60], attention-based KD [61], and graph-based KD [62].

While the effectiveness of existing KD methods has been validated in general vision tasks, current methods mainly rely on coarse task-agnostic knowledge and do not consider the task-specific feature requirements [24], [50], [63]–[65]. Especially for EDIPs, models are highly sensitive to feature representations [1], [40], [66], [67]. Therefore, general KD may not be effective enough and can be considered purposeless and redundant [18], [24], [25], [45], remaining a performance gap between the obtained results and the expected ones [19], [26], [68]. Recent studies have shown that task-specific patterns of KD can help further improve the performance of student models [69]. For example, in object detection, object localization KD leads to more accurate predictions than the general knowledge [63], [70]. In this work, we also adopt the idea of task-specific KD. Our contribution lies in proposing a customized KD scheme, namely boundary distillation and context distillation, which target the common errors of EDIP models, namely their tendency to make errors in *maintaining boundary region completeness* and *ensuring target region connectivity*. It is also worth noting that while some advanced methods, *e.g.*, CTO [71], SlimSeg [72], and BPKD [73], have integrated boundary information in EDIPs, *they necessitate the pre-extraction and incorporation of ground-truth boundary information* [71]–[73]. In contrast, our method obviates the demand for pre-extracting object boundaries, thereby making it more practical for real-world applications and enabling savings in time and labor.

III. PRELIMINARIES

In the training phase, KD intends to facilitate expectant knowledge transfer from a large teacher model \mathbb{T} to a small compact student model \mathbb{S} , with the primary goal of enhancing the accuracy of \mathbb{S} [14], [16], [24], [59], [74]. In inference, only \mathbb{S} is used, so there are no computational overheads. Typically, features and logits serve as a medium for knowledge transfer. Besides, the temperature scaling strategy is often utilized to smooth the features and logits, which helps to lower prediction confidence and alleviate the issue of excessive self-assurance in \mathbb{T} [75]. Formally, KD can be expressed by minimizing the cross-entropy loss as follows:

$$\mathcal{L}_{KD} = -\tau^2 \sum_{i \in M} \sigma(\mathbf{T}_i)^{1/\tau} \log \left(\sigma(\mathbf{S}_i)^{1/\tau} \right), \quad (1)$$

where \mathbf{T}_i and \mathbf{S}_i (both have been adjusted to the same dimension via 1×1 convolutions) are the i -th feature/logit item extracted from \mathbb{T} and \mathbb{S} , respectively. $\sigma(\cdot)$ is the softmax normalization operation along the channel dimension, and $\tau \in \mathbb{R}_+$ denotes the temperature scaling coefficient. M denotes the learning objective of \mathbf{T}_i and \mathbf{S}_i , which typically refers to the spatial dimensions. Following [59], [75], to simplify temperature scaling effectively, we use $\mathbf{T}_i/\mathbf{S}_i$ divided by τ to achieve the similar effect. In addition to cross-entropy loss, other loss functions are also commonly used for KD, including KL divergence loss and MSE loss [76]–[78]. While existing KD methods have demonstrated promising results across various vision tasks [14], [19], [20], [24], [25], [76], they have not adequately addressed the specific feature understanding required for object boundaries and connecting regions in EDIP tasks. This oversight has led to suboptimal performance in these contexts. In following, we will introduce a complementary and targeted KD scheme informed by the common failure cases observed in small models, as shown in Figure 1, with the aim of enhancing their inference accuracy.

IV. OUR METHOD

A. Overview

Figure 2 illustrates an overview of the network architecture for our proposed BCKD. The whole network mainly consists of an accurate teacher network \mathbb{T} , which is a large network that has been trained, and a small efficient network \mathbb{S} that is waiting to be trained. The input for \mathbb{T} and \mathbb{S} is an arbitrary RGB image \mathbf{X} , and the output of \mathbb{S} is a semantic mask or bounding box \mathbf{Y} that predicts each pixel or/and object with a specific class label. The hierarchical features extracted from the backbone network are concatenated along the channel dimension to facilitate the extraction of EDIP-specific boundary and contextual information from \mathbf{X} . The concatenated features with 256 channel dimension are defined as $\mathbf{T}^c = \text{Conv}_{3 \times 3}(\text{concat}(\mathbf{T}_1; \mathbf{T}_2; \dots; \mathbf{T}_5))$ and $\mathbf{S}^c = \text{Conv}_{3 \times 3}(\text{concat}(\mathbf{S}_1; \mathbf{S}_2; \dots; \mathbf{S}_5))$ for \mathbb{T} and \mathbb{S} , respectively. It should be noted that both \mathbf{T}_i and \mathbf{S}_i that are concatenated have been uniformly resized into $1/8$ of \mathbf{X} 's spatial size via 1×1 convolution and up-/down-sampling operations. In training, we propose targeted *boundary distillation* and *context distillation* strategies that are tailored for the EDIP tasks. Specifically, the *boundary distillation* synthesizes

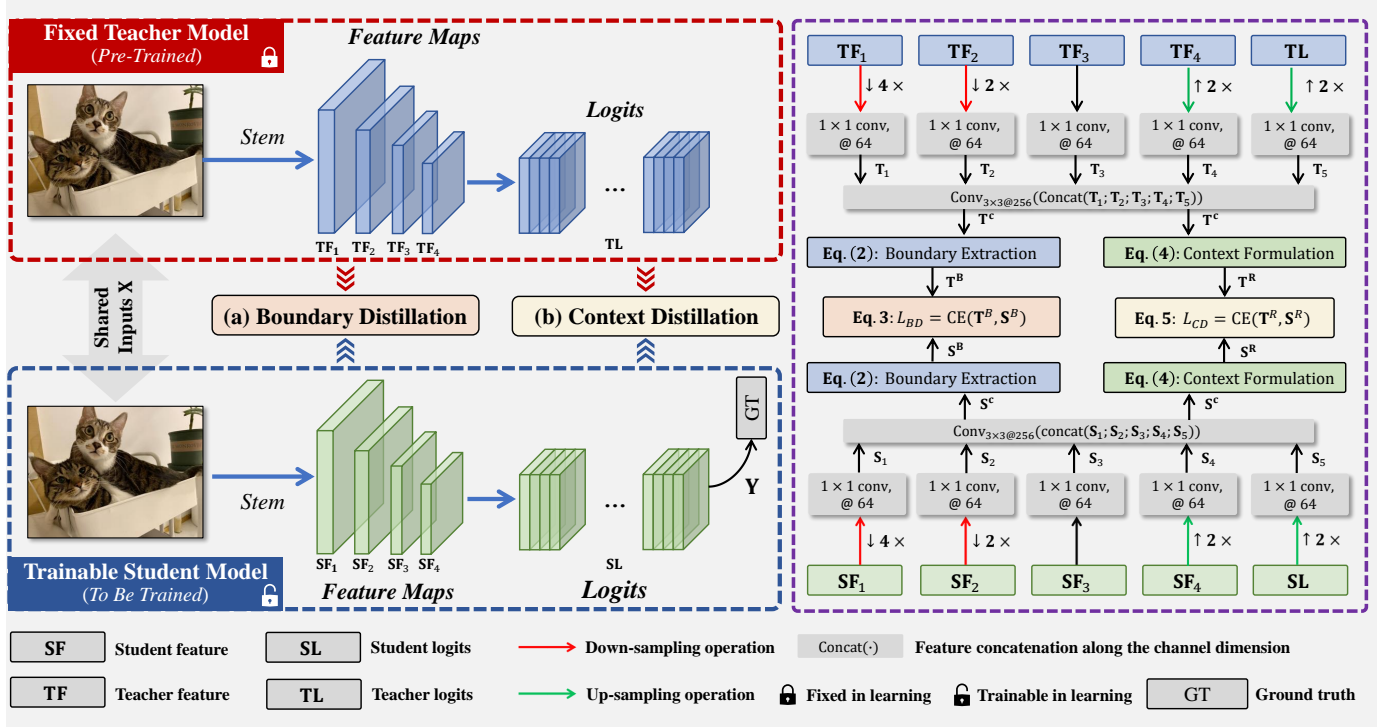


Figure 2. The overall network architecture of our proposed boundary and context distillation strategy for the efficient dense image prediction tasks, where the right side illustrates the implementation details of the whole network. Specifically, the boundary distillation involves generating explicit object-level boundaries from the hierarchical backbone features, enhancing the completeness of the student model’s masks in boundary regions (*ref.* Sec. IV-B). At the same time, the context distillation transfers implicit pixel-level contexts from the teacher model to the student model through self-relations, ensuring robust connectivity in the student’s masks (*ref.* Sec. IV-C). Compared to existing methods, our method demonstrates a stronger specificity for the EDIP tasks and inherently possesses the ability to synergistically address the common errors found in small models.

explicit object-level boundaries \mathbf{T}^B and \mathbf{S}^B from \mathbf{T}^c and \mathbf{S}^c , respectively, thereby the completeness of \mathbf{S} ’s results in the boundary regions can be enhanced. At the same time, the *context distillation* transfers implicit pixel-level relations \mathbf{T}^R and \mathbf{S}^R by using self-relations, ensuring that \mathbf{S} ’s results have strong target region connectivity.

B. Boundary Distillation

The semantic object boundary is defined as a set of arbitrary pixel pairs from the given image, where the boundary between pairwise pixels has a value of 1 if they belong to different classes, while if the pairwise pixels belong to the same class, the boundary between them has a value of 0 [79]. Moreover, this attribute also exists in the hierarchical features/logits extracted by the backbone feature maps [80]. In our work, we use the semantic affinity similarity between arbitrary pairwise pixels from \mathbf{T}^c or \mathbf{S}^c to obtain the explicit object-level boundaries [5], [81]. Concretely, for a pair of image pixels \mathbf{T}_i^c and \mathbf{T}_j^c , $\mathbf{T}_{i,j}^B$ can be formulated as:

$$\mathbf{T}_{i,j}^B = 1 - \max_{p,q \in \Pi_{i,j}} \mathcal{B}(\text{Conv}_{1 \times 1}(\mathbf{T}_i^c p), \text{Conv}_{1 \times 1}(\mathbf{T}_j^c q)), \quad (2)$$

where \mathbf{T}_p^c and \mathbf{T}_q^c are two arbitrary pixel items from \mathbf{T}^c , and $\Pi_{i,j}$ denotes a set of pixel items on the line between \mathbf{T}_i^c and \mathbf{T}_j^c . $\text{Conv}_{1 \times 1}$ denotes a 1×1 convolution layer that is used to compress the channel dimension, where the input channel size is 256 and output channel size is 1. $\mathcal{B}(\cdot)$ denotes the operation that determines the object-level image boundary values, which

outputs either 1 or 0. \mathbf{T}^B can be obtained across the entire spatial domain, and \mathbf{S}^B can be obtained analogously. Based on \mathbf{T}^B and \mathbf{S}^B , boundary distillation loss is formulated as:

$$\mathcal{L}_{BD} = -\tau^2 \sum_{i \in M} \rho(\mathbf{T}_i^B)^{1/\tau} \log(\rho(\mathbf{S}_i^B)^{1/\tau}), \quad (3)$$

where ρ denotes the spatial-wise softmax normalization. By Eq. (3), \mathbf{T} ’s accurate prediction of the object boundary region can be transferred into \mathbf{S} , thereby addressing its issue of maintaining boundary region completeness.

The proposed boundary distillation strategy can effectively address the limitations of EDIP models in achieving completeness in boundary region predictions. *It is important to highlight that while several advanced methods, such as BGLSSeg [32], SlimSeg [72], and BPKD [73], leverage explicit edge information for semantic segmentation, these methods necessitate the pre-extraction and integration of ground-truth masks (please refer to Table III for further details). More importantly, the extracted edge information often lacks the semantic context of the objects and may introduce noise [82], [83].* In contrast, our method eliminates the need for pre-extracting image edges. By utilizing hierarchical feature maps, our method enhances the delineation of object boundaries with more comprehensive semantic information while mitigating the adverse effects of noise present in shallow features. As illustrated in Figure 3, we show a comparison of the extracted image boundaries between our method and the ground truth edge method used in the state-of-the-art BPKD [73] model. We can observe that

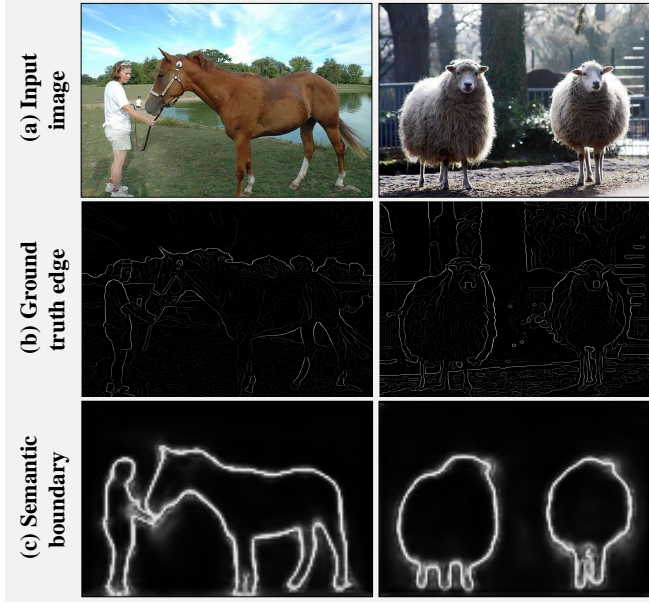


Figure 3. The visualization comparisons of the extracted image boundaries between our method in (c) and the ground truth edge method in (b) used in the state-of-the-art BPKD [73]. Images are from Pascal VOC 2012 [28].

the semantic boundaries extracted by our method can better cover the actual boundaries of the semantic objects without introducing background noise information. This innovation not only can enhance the practicality of our method for real-world applications but also streamlines the overall process, leading to reductions in both time and labor requirements.

C. Context Distillation

Elaborate object relations, as validated in [84]–[86], are beneficial for learning implicit contextual information across spatial dimensions [83], [87]. In this paper, we also adopt this scheme to address the challenge of inadequate preservation of target region connectivity in EDIPs. We consider this scheme as the medium in the KD process. Our contribution lies in treating pixel-level relations as a bridge for context transfer. Compared to existing methods [83], [86], our approach utilizes pixel-level relations solely during the training process, thereby avoiding the increase in model complexity and parameters in inference that is typically associated with current methods [76], [87]. Besides, compared to object-level relations, the employed pixel-level relations can capture global contextual information more comprehensively, making them more suitable for DIP tasks. Specifically, for the concatenated features \mathbf{T}^c of \mathbb{T} , its self-relation \mathbf{T}^R is formulated as:

$$\mathbf{T}^R = \sigma \left(\frac{O(\mathbf{T}^c)^T \cdot O(\mathbf{T}^c)}{\sqrt{d}} \right) / \tau \in \mathbb{R}^{hw \times hw}, \quad (4)$$

where $O(\cdot)$ denotes the feature-aligned operation as in [86], [88], which aims to align the feature distribution of the \mathbb{S} with that of the \mathbb{T} as closely as possible. T denotes the matrix transpose operation. d is the channel size of \mathbf{T}^c , which is 256. h and w denotes the height and width of \mathbf{T}^c , respectively. \mathbf{S}^R

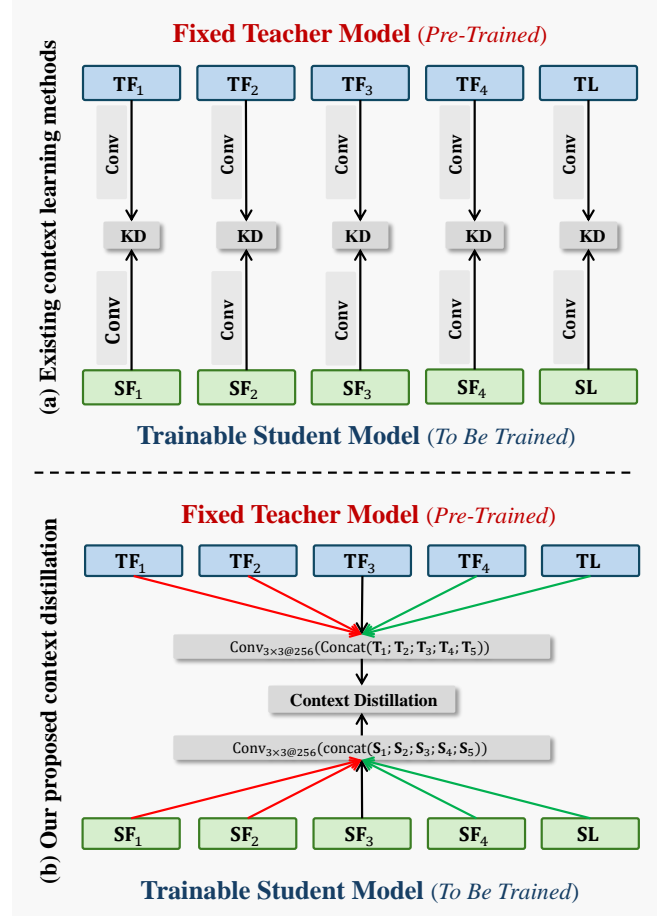


Figure 4. Architecture comparisons between our proposed context distillation (b) and existing context learning methods (a). Our method leverages concatenated features in a whole-to-whole manner, which avoids the potential noise introduced by layer-to-layer distillation modes.

of \mathbb{S} can also be obtained analogously. Therefore, the *context distillation* can be expressed as:

$$\mathcal{L}_{CD} = -\tau^2 \sum_{k \in hw \times hw} \sigma(\mathbf{T}_k^R)^{1/\tau} \log \left(\sigma(\mathbf{S}_k^R)^{1/\tau} \right), \quad (5)$$

where $k = (1, 2, \dots, hw \times hw)$ is the index item. \mathbf{T}_k^R and \mathbf{S}_k^R denotes the k -th item in \mathbf{T}^R and \mathbf{S}^R , respectively.

The proposed context distillation method presents an efficient solution that does not incur additional inference overhead. As illustrated in Figure 4, our method in (b), which utilizes concatenated features in a whole-to-whole manner, circumvents the potential noise associated with existing context learning methods in (a) for semantic segmentation [73], [76] that rely on layer-to-layer distillation. Our method is specifically tailored to address the potential challenge of incomplete preservation of target region connectivity as shown in Figure 1, rather than solely focusing on the enhancement of feature representations in a generic context.

D. Overall Loss Function

With the boundary distillation loss \mathcal{L}_{BD} and the context distillation loss \mathcal{L}_{CD} , the total loss can be expressed as:

$$\mathcal{L} = \mathcal{L}_{SS} + \alpha \mathcal{L}_{BD} + \beta \mathcal{L}_{CD}, \quad (6)$$

where α and β are two weights used to balance different losses. Empirically, these weights have a significant impact on model performance, and unreasonable weight settings may even lead to model collapse in training. To this end, inspired by previous work [63], [89], to enhance the dependence of \mathbb{S} on ground truth labels, we incorporate a weight-decay strategy that promotes a greater focus on \mathcal{L}_{SS} as the training epoch increases. To this end, we initialize a time function as follows:

$$r(t) = 1 - (t - 1)/t_{\max}, \quad (7)$$

where $t = (1, 2, \dots, t_{\max})$ denotes the current training epoch and t_{\max} is the maximum training epoch. In training, we control the dependence of \mathcal{L} on \mathcal{L}_{BD} and \mathcal{L}_{CD} by using $r(t)$. Therefore, the total loss in Eq. (6) can be formulated as:

$$\mathcal{L} = \mathcal{L}_{SS} + r(t)\alpha\mathcal{L}_{BD} + r(t)\beta\mathcal{L}_{CD}. \quad (8)$$

E. Theoretical Analysis

Our BCKD is theoretically grounded in differential geometry and spectral graph theory. In the following, we will analyze its components through measurable properties of the learned feature manifolds \mathcal{M}_T (teacher) and \mathcal{M}_S (student), with proofs connecting to the empirical results in Section V-C. **Boundary-Aware Manifold Alignment.** The proposed \mathcal{L}_{BD} in Eq. (3) induces geometric consistency between teacher and student decision boundaries.

Theorem 1 (Boundary Consistency). *Under \mathcal{L}_{BD} minimization with $\tau > 1$, for any boundary point x_b , we have:*

$$\|\mathbf{J}_T(x_b) - \mathbf{J}_S(x_b)\|_F \leq \sqrt{2\mathcal{L}_{BD}/\tau^2} + \mathcal{O}(e^{-\tau}), \quad (9)$$

where \mathbf{J}_\cdot are Jacobian matrices of the feature maps.

Proof. The temperature-scaled gradients satisfy:

$$\nabla \mathcal{L}_{BD} = \mathbb{E}_{x_b} \left[\frac{\sigma_T^{1/\tau}}{\sigma_S^{1/\tau}} \nabla \log \sigma_S \right], \quad (10)$$

$$\|\nabla L_T - \nabla L_S\|^2 \leq 2(1 - \cos \theta), \quad (11)$$

where θ is the angle between \mathbb{S} and \mathbb{T} gradients. Applying Taylor expansion [90] at high τ , then we can obtain:

$$\cos \theta \geq 1 - \frac{1}{2}\mathcal{L}_{BD}\tau^{-2} + \mathcal{O}(\tau^{-4}). \quad (12)$$

The Jacobian bound follows from Pinsker's inequality applied to the manifold tangent spaces. \square

This theoretical guarantee explains the 0.91% mIoU improvement observed in Table I, as aligned Jacobians ensure consistent boundary localization.

Contextual Graph Preservation The proposed \mathcal{L}_{CD} in Eq. (5) maintains spectral properties critical for dense image prediction tasks:

Theorem 2 (Spectral Convergence). *For eigenvalues $\{\lambda_i\}$ of relation matrices $\mathbf{T}^R, \mathbf{S}^R$, we have:*

$$\max_i |\lambda_i^T - \lambda_i^S| \leq \|\mathbf{T}^R - \mathbf{S}^R\|_F \leq \sqrt{d}\mathcal{L}_{CD}. \quad (13)$$

Proof. Applying Weyl's inequality for symmetric matrices, we can obtain:

$$|\lambda_i^T - \lambda_i^S| \leq \|\Delta \mathbf{R}\|_2 \leq \|\Delta \mathbf{R}\|_F, \quad (14)$$

where the heat kernel continuity follows from:

$$\|e^{-\tau\mathcal{L}_T} - e^{-\tau\mathcal{L}_S}\|_F \leq \tau \sup_{t \in [0, \tau]} \|e^{-t\mathcal{L}_T}(\mathcal{L}_T - \mathcal{L}_S)e^{-(\tau-t)\mathcal{L}_S}\| \quad (15)$$

$$\leq \tau e^{\tau\|\mathcal{L}_T\|} \mathcal{L}_{CD} \quad (16)$$

\square

As shown in Table I, compared with the baseline model, the 1.77% mIoU gain directly reflects this eigenvalue stability.

Multi-Scale Geometric Consistency As illustrated in Figure 4, the feature concatenation and projection operation in Section IV-A preserves topological invariants:

Proposition 1 (Topological Preservation). *The mapping $\phi : \prod_i \mathcal{M}_T^{(i)} \rightarrow \mathcal{M}_T^{\text{concat}}$ satisfies:*

$$\beta_k(\mathcal{M}_T^{\text{concat}}) = \sum_{i=1}^5 \beta_k(\mathcal{M}_T^{(i)}), \quad k = 0, 1, 2 \quad (17)$$

where β_k are Betti numbers.

Proof. The 3×3 convolution operation is a diffeomorphism, thus we have:

$$\beta_k(\phi(\mathbf{T}^c)) = \beta_k(\mathbf{T}^c) \quad (\text{invariance}) \quad (18)$$

$$= \beta_k(\oplus_i \mathcal{M}_T^{(i)})$$

$$= \sum_{i=1}^5 \beta_k(\mathcal{M}_T^{(i)}) \quad (\text{K\"unneth formula}) \quad (19)$$

The dimensionality bound follows from the classical projection theorem as in [91]. \square

Training Dynamics Interpretation The used weight decay in Eq. (8) induces phased learning:

Theorem 3 (Annealed Convergence). *With $r(t) = 1 - (t - 1)/t_{\max}$ and Robbins-Monro conditions on learning rate η_t :*

$$\lim_{t \rightarrow t_{\max}} \mathbb{P}(\mathcal{L} = \mathcal{L}_{SS}) = 1 \quad (20)$$

Proof. Decompose the gradient flow:

$$\begin{aligned} \frac{d\mathcal{L}}{dt} &= -\eta_t \|\nabla \mathcal{L}_{SS}\|^2 \\ &\quad - \eta_t r(t)^2 (\alpha^2 \|\nabla \mathcal{L}_{BD}\|^2 + \beta^2 \|\nabla \mathcal{L}_{CD}\|^2) \end{aligned} \quad (21)$$

As $r(t) \rightarrow 0$, the right terms vanish asymptotically. The convergence follows the stochastic approximation theory [92]. \square

V. EXPERIMENTS

A. Datasets and Evaluation Metrics

1) *Datasets:* To demonstrate the superior performance of our method, we conduct experiments on five representative yet challenging datasets: Pascal VOC 2012 [28], Cityscapes [29], ADE20K [12], and COCO-Stuff 10K [30] for semantic segmentation (SSeg), as well as MS-COCO 2017 [31] for instance segmentation (ISeg) and object detection (ODet).

- The Pascal VOC 2012 dataset comprises 20 object classes along with one background class. Following [14], [20], we utilized the augmented data, resulting in a total of 10,582 images for *training*, 1,449 images for *val*, and 1,456 images for *testing*.
- The Cityscapes dataset comprises a total of 5,000 finely annotated images, which are partitioned into subsets of 2,975, 500, and 1,525 images designated for *training*, *val*, and *testing*, respectively. In alignment with existing methods [20], [76], [78], we exclusively employed the finely labeled data during the training phase to ensure a fair comparison of results.
- The ADE20K dataset has 150 object classes and is organized into three subsets: 20,000 images for the *training* set, 2,000 images for the *val* set, and 3,000 images for the *testing* set.
- The COCO-Stuff 10K dataset is an extension of the MS-COCO dataset [31], enriched with pixel-wise class labels. It consists of 9,000 samples designated for *training* and 1,000 samples allocated for *val*.
- The MS-COCO 2017 dataset comprises 80 object classes and includes a total of 118,000 images for *training*, and 5,000 images for *val*.

For data augmentation, random horizontal flip, brightness jittering and random scaling within the range of $[0.5, 2]$ are used in training as in [14], [20], [76]. Experiments are implemented on the MMRazor framework² under the PyTorch platform [93] using 8 NVIDIA GeForce RTX 3090 GPUs. All the inference results are obtained at a single scale.

2) *Evaluation metrics*: Beyond employing standard metrics, we have also developed two extra specialized evaluation metrics specifically optimized for knowledge distillation on dense image prediction tasks, detailed below:

Common metrics. For SSeg, we utilize the mean intersection over union (mIoU) as the primary evaluation metric. For ISeg and ODet, average precision (AP) serves as the principal accuracy-specific metric. To assess model efficiency, we also consider the number of parameters (Params.) and the floating-point operations (FLOPs).

Manifold stability (MFS). To assess the effectiveness on the learned feature manifolds, we compute the Lipschitz constant ratio between teacher and student models. Specifically, let $f_T^l(x), f_S^l(x) \in \mathbb{R}^{d_l}$ denote the l -th layer feature mappings for teacher and student models respectively. The layer-wise Lipschitz constant is estimated via:

$$L_k^l = \sup_{x \in \mathcal{X}, \|\delta\| \leq \epsilon} \frac{\|f_k^l(x + \delta) - f_k^l(x)\|_2}{\|\delta\|_2}, \quad k \in \{T, S\} \quad (22)$$

where \mathcal{X} is the input space and $\epsilon = 0.1$ controls the perturbation scale. The MFS metric ρ_l is then computed as:

$$\rho_l = \frac{L_S^l}{L_T^l} \cdot \mathbb{I}(L_T^l > \tau) + \mathbb{I}(L_T^l \leq \tau) \quad (23)$$

with threshold τ avoiding division by negligible values ($\tau = 0.01$). Values close to 1 indicate well-preserved manifold structure during distillation, while significant deviations suggest potential degradation of geometric properties.

Local Hausdorff distance (LHD). For boundary-sensitive tasks like SSeg and ISeg, we introduce a LHD measure to evaluate boundary alignment quality. Specifically, for boundary point sets $\mathcal{B}_p = \{p_i\}_{i=1}^m$ and $\mathcal{B}_g = \{q_j\}_{j=1}^n$, the LHD at point p_i is defined as:

$$\text{LHD}_r(p_i, \mathcal{B}_g) = \min \left\{ \max_{q_j \in N_r(p_i)} d(p_i, q_j), \text{median}(\{d(p_i, q_j)\}_{q_j \in N_r(p_i)}) \right\}, \quad (24)$$

where the neighborhood $N_r(p_i)$ and final aggregation are:

$$\begin{aligned} N_r(p_i) &= \{q_j \in \mathcal{B}_g \mid \|p_i - q_j\|_2 \leq r\} \\ \text{LHD}(\mathcal{B}_p, \mathcal{B}_g) &= \frac{1}{|\mathcal{B}_p|} \sum_{i=1}^{|\mathcal{B}_p|} \text{LHD}_r(p_i, \mathcal{B}_g) \\ &\quad \cdot \mathbb{I}(\text{LHD}_r(p_i, \mathcal{B}_g) \leq \mu + 2\sigma), \end{aligned} \quad (25)$$

where r is set to 5 in our implementation.

B. Implementation Details

1) *Baselines*: For a fair result comparison and considering the realistic resource conditions of edge computing devices [54], **for SSeg**, we select **PSPNet-101** [27], **DeepLabv3 Plus-101** [94], and **Mask2Former** [8] for the teacher models. The student models are compact **PSPNet** and **DeepLabV3+** with ResNet-38, ResNet-18_(0.5) and ResNet-18_(1.0) [95]. Besides, to demonstrate the superior effectiveness of our method on heterogeneous network architectures, following [20], [68], [76], we also employ **MobileNetV2** [96], **EfficientNet-B1** [97], and **SegFormer-B0** [47] as the student models. **For ISeg and ODet**, following [26], [98], we select the representative **GFL** [99], **Cascade Mask R-CNN** [100], and **RetinaNet** [101] with ResNet-101/50 and ResNet-50/18 as the teacher model and the student model, respectively. *While adopting cutting-edge large foundation models represents the prevailing research trend, we opt for a pragmatic small-model baseline given the currently insurmountable challenges in deploying such large-scale models on edge devices. This application-oriented approach prioritizes practical deployability over model scale, while still providing a meaningful benchmark for edge computing scenarios.* During the training and inference phases, aside from our proposed method and specific declarations, all other settings adhere to the configurations outlined in the baseline model.

2) *Training details*: Following the standard practices as in [16], [20], [76], all teacher models are pre-trained on ImageNet-1k by default [102], and then fine-tuned on the corresponding dataset before their parameters are fixed in KD. During training, only the student's parameters are updated. As in [14], [75], τ is initialized to 1 and is multiplied by a scaling factor of 1.05 whenever the range of values (across all feature items in a given minibatch) exceeds 0.5. Following [20], [63], [89], α and β is set to 10 and 50, respectively. We fully understand that fine-tuning these base hyperparameters could potentially enhance performance. However, we contend that such adjustments may be redundant and unwarranted.

For SSeg models, to accommodate the local hardware limitations, the training images are cropped into a fixed size of

²<https://github.com/open-mmlab/mmrazor>

Table I
ABLATION RESULTS ON THE *val* SET OF PASCAL VOC 2012 [28] BY
ADDING EACH COMPONENT OF BCKD. “WD” DENOTES THE
WEIGHT-DECAY STRATEGY AS INTRODUCED IN SECTION IV-D

T: PSPNet-101 [27]			77.82 %	70.43M	411.6G
S: PSPNet-18 _(1.0) [27]			70.78 %	15.24M	106.2G
\mathcal{L}_{BD}	\mathcal{L}_{CD}	WD	mIoU (%)	Params.	FLOPs
✓	✗	✗	71.69 ^{+0.91}	15.24M	106.2G
✗	✓	✗	72.55 ^{+1.77}	15.24M	106.2G
✓	✓	✗	73.98 ^{+3.20}	15.24M	106.2G
✓	✓	✓	74.65 ^{+3.87}	15.24M	106.2G



Figure 5. Visualized comparisons and results obtained by adding different components of BCKD. The teacher model and the student model denotes PSPNet-101 [27] and PSPNet-18_(1.0) [27], respectively. “w/” denotes with the corresponding implementation. Samples are from Pascal VOC 2012 [28].

512 × 512 pixels as in [26], [98]. The SGD is used as the optimizer with the “poly” learning rate strategy. The initial learning rate is set to 0.01, with a power of 0.9. To ensure fairness in the experimental comparisons, the batch size is set to 8 and t_{\max} is set to 40,000.

For ISeg and ODet, the model is trained following the default 1 × training schedule, *i.e.*, 12 epochs. The batch size is set to 8, and AdamW is used as the optimizer with the initial learning rate of 1×10^{-4} and the weight decay of 0.05. The layer-wise learning rate decay is used and set to 0.9, and the drop path rate is set to 0.4. The given images are resized to the shorter side of 800 pixels, with the longer side not exceeding 1,333 pixels. In inference, the shorter side of images is consistently set to 800 pixels by default.

C. Ablation Analysis

In our ablation analysis, we aim to explore answers of the following crucial questions: 1) the impact of each component within BCKD; 2) the effectiveness of BCKD across different network architectures; and 3) the visualized performance and comparisons with other methods. We select the SSeg task as the experimental objective.

1) *Effectiveness of each component*: To explore answer of the first question, we chose Pascal VOC 2012 [28] as the experimental dataset. PSPNet-101 [27] serves as the teacher

Table II
RESULT COMPARISONS ON mIoU (%) UNDER DIFFERENT NETWORK
ARCHITECTURES ON THE *val* SETS OF PASCAL VOC 2012 [28],
CITYSCAPES [29], AND ADE20K [12], AND ON THE *test* SET OF
COCO-STUFF 10K [30].

Methods	Pascal VOC <i>val</i>	Params.
DANet [22]	80.40	83.1M
T: PSPNet-101 [27]	77.82	70.4M
S: PSPNet-38 [27]	72.65	58.6M
+ BCKD _{ours}	75.15 ^{+2.50}	58.6M
S: EfficientNet-B1 [97]	69.28	6.7M
+ BCKD _{ours}	73.81 ^{+4.53}	6.7M
S: SegFormer-B0 [47]	66.75 [‡]	3.8M
+ BCKD _{ours}	68.88 ^{+2.13}	3.8M
Methods	Cityscapes <i>val</i>	Params.
HRNet [103]	81.10	65.9M
T: PSPNet-101 [27]	78.56	70.4M
S: PSPNet-38 [27]	71.26	47.4M
+ BCKD _{ours}	73.56 ^{+2.30}	47.4M
S: EfficientNet-B1 [97]	60.40	6.7M
+ BCKD _{ours}	63.91 ^{+3.51}	6.7M
S: SegFormer-B0 [47]	76.20	3.8M
+ BCKD _{ours}	77.87 ^{+1.67}	3.8M
Methods	ADE20K <i>val</i>	Params.
DeepLab V3 [104]	43.28	71.3M
T: PSPNet-101 [27]	42.19	70.4M
S: ESPNet [105]	20.13	0.4M
+ BCKD _{ours}	23.65 ^{+3.52}	0.4M
S: MobileNetV2 [96]	33.64	8.3M
+ BCKD _{ours}	36.59 ^{+2.95}	8.3M
S: SegFormer-B0 [47]	37.40	3.8M
+ BCKD _{ours}	38.75 ^{+1.35}	3.8M
T: Mask2Former [8]	47.20	44.0M
S: ESPNet + BCKD _{ours}	24.26 ^{+4.13}	0.4M
S: MobileNetV2 + BCKD _{ours}	37.09 ^{+3.45}	8.3M
S: SegFormer-B0 + BCKD _{ours}	39.61 ^{+2.21}	3.8M
Methods	COCO 10K <i>test</i>	FLOPs
SegViT [106]	50.3	383.9G
T: DeepLabV3 Plus-101 [94]	33.10	366.9G
S: MobileNetV2 [96]	26.29	1.4G
+ BCKD _{ours}	28.31 ^{+2.02}	1.4G
S: SegFormer-B0 [47]	35.60	8.4G
+ BCKD _{ours}	35.92 ^{+0.32}	8.4G

model, while PSPNet-18_(1.0) is used as the student model. Table I shows the inference results by adding each component of BCKD into the student model, where we report the experimental results on the *val* set. We can observe that incorporating these components consistently improves the model accuracy, indicating the effectiveness of these components. In particular, adding \mathcal{L}_{BD} resulted in a mIoU \uparrow gain of 0.91%, which may be attributed to the fact that the object boundary regions are relatively small in proportion to the entire image [14], [73]. With only the implementation of \mathcal{L}_{BD} and \mathcal{L}_{CD} , our model can achieve the competitive 73.98% mIoU with 3.20% mIoU \uparrow improvements, which verifies the importance of boundary and context information in EDIP. Furthermore, this result demonstrates that our \mathcal{L}_{BD} and \mathcal{L}_{CD} do not conflict in practical deployment; instead, they complement each other intrinsically to enhance performance. It is also worth noting that compared to the advanced methods in Table III that do not utilize ground

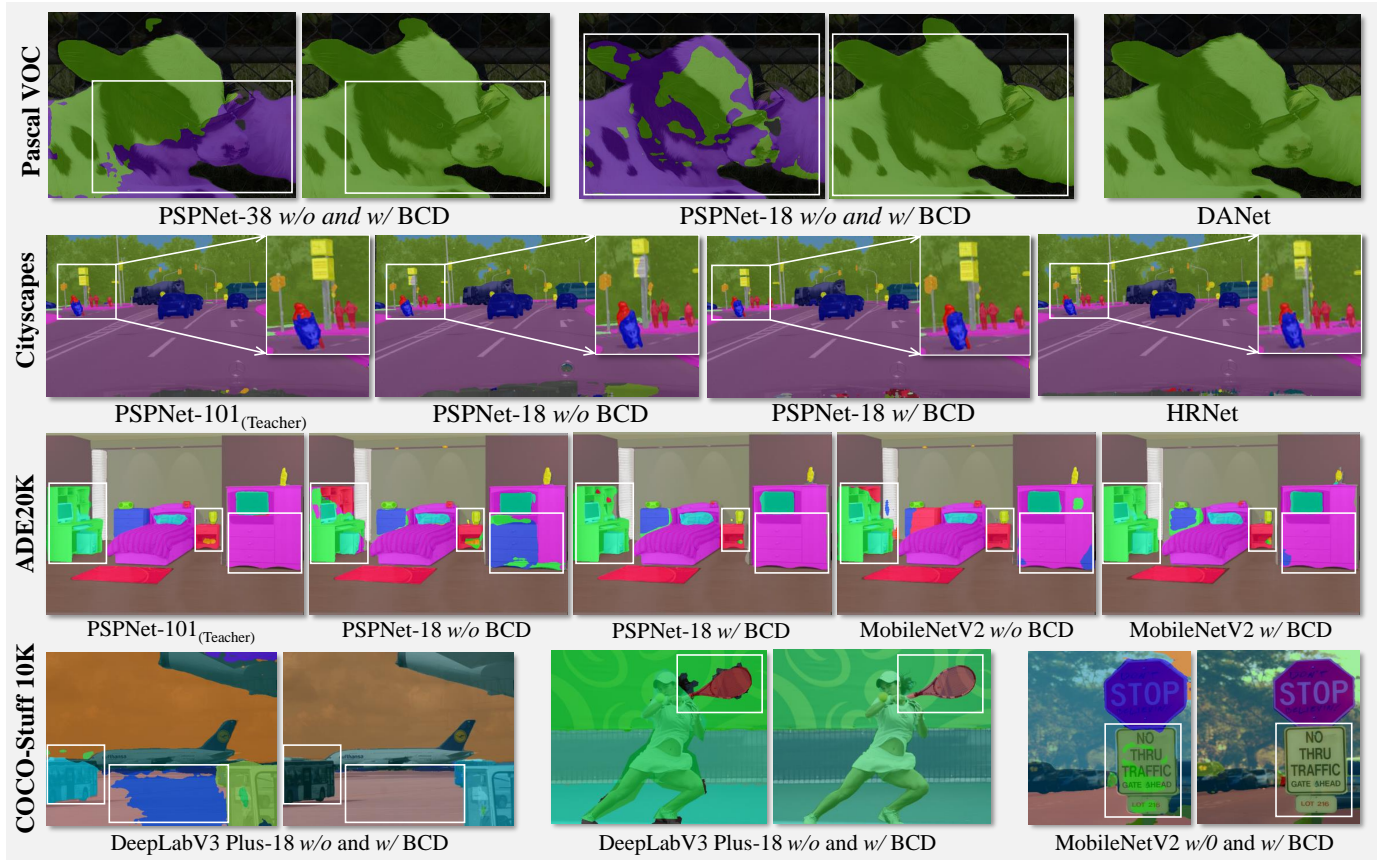


Figure 6. Visualizations on SSeg. DANet [22] and HRNet [103] have been included for comparison as well. “w/o” means “without” and “w/” means “with”, indicating whether our method is NOT implemented or implemented. The white bounding boxes highlight the regions where our method predicts better.

truth mask, our method also achieves competitive results even without employing the weight-decay strategy. Building upon \mathcal{L}_{BD} and \mathcal{L}_{CD} , adding the weight-decay strategy brings 0.57% mIoU \uparrow , which confirms the weight importance of different losses. Furthermore, there is no increase in the number of Params. or FLOPs in the inference stage.

We also employ visualizations as a means of verifying the efficacy of BCKD components incrementally into the baseline model. The obtained results are presented in Figure 5, which demonstrate that the inclusion of \mathcal{L}_{BD} and \mathcal{L}_{CD} in a sequential manner leads to enhanced boundary regions and object connectivity. For example, the “bike handlebar”. Moreover, the integration of the weight-decay strategy results in further improvement in the overall segmentation predictions. In addition to using white bounding boxes to emphasize the better regions achieved by our method, we also highlighted the regions of prediction failure using red dashed bounding boxes. We can observe that although our BCKD significantly improves the prediction quality of these regions compared to the student model’s results, there are still some incomplete predictions. This case may be caused by the spurious correlation between the “helmet” and the “person” in the used dataset, which can be eliminated through causal intervention [4].

2) *Effectiveness across network architectures*: In this section, we evaluate the effectiveness of our BCKD across various network architectures for SSeg using: Pascal VOC 2012 [28], Cityscapes [29], ADE20K [12], and COCO-Stuff 10K [30]. The obtained results under different network architectures

are given in Table II. For the purpose of comparing experimental results, we also include the results of a large model that does not utilize knowledge distillation for each dataset. From this table, we can observe that deploying BCKD on different network architectures can lead to continuous performance improvements. For example, when employing PSPNet-38 [27], EfficientNet-B1 [97], and SegFormer-B0 [47] as student models while keeping the teacher model PSPNet-101 [27] unchanged, our BCKD achieves mIoU \uparrow improvements of 2.50%, 4.53%, and 2.13% on Pascal VOC *val*, and 2.30%, 3.51%, and 1.67% on Cityscapes *val*, respectively. The performance gains demonstrate the effectiveness of our method not only within the same network architecture but also across network architectures, indicating sustained performance enhancements. This phenomenon also highlights the generalization capacity of our method. Besides, similar conclusions can be also drawn from our experimental results on ADE20K *val* and COCO-Stuff 10K *test* sets. Deploying different teacher models on the ADE20K *val* dataset are also conducted, where Mask2Former [8] is utilized as the teacher model, and ESPNet [105], MobileNetV2 [96], and SegFormer-B0 are used as the student models. The results demonstrate that our method yields mIoU \uparrow improvements of 4.13%, 3.45%, and 2.21% on ESPNet, MobileNetV2, and SegFormer-B0 [47], respectively, showcasing the strong flexibility. On efficiency, our method leverages the KD framework, resulting in no increase in Params. or FLOPs. Consequently, we achieve both improved accuracy and fast inference speed.

Table III

COMPARISONS ON mIoU (%) WITH STATE-OF-THE-ART METHODS ON THE *val* SETS OF PASCAL VOC 2012 [28] AND CITYSCAPES [29], AND ADE20K [12]. “ \ddagger ” DENOTES OUR RE-IMPLEMENTED RESULT BASED ON THE RELEASED CODES DUE TO INCONSISTENCIES IN EXPERIMENTAL SETTINGS. “KD MANNER”: KNOWLEDGE DISTILLATION MANNER, WHICH CONTAINS OF LAYER-TO-LAYER (L2L) AND WHOLE-TO-WHOLE (W2W) AS ILLUSTRATED IN FIGURE 4. “GROUND-TRUTH MASK”: GROUND-TRUTH MASK USED TO OBTAIN THE PRE-EXTRACTION IMAGE BOUNDARIES. “E”: PHYSICAL EDGE. “B”: SEMANTIC BOUNDARY. “P”: PIXEL-WISE. “I”: IMAGE-WISE. “O”: OBJECT-WISE.

T: PSPNet-101 [27]					77.82%	78.56%	42.19%
S: PSPNet-18 _(1.0) [27]					70.78%	69.10%	33.82%
Methods	KD Manner	Ground-truth mask?	Boundary type	Context type	Pascal VOC 2012	Cityscapes	ADE20K
+ KD [16]	L2L	\times	\times	\times	71.28 \ddagger +0.50	71.20+2.10	34.33 \ddagger +0.51
+ SKD [76]	L2L	\checkmark	E	P	73.05+2.27	71.45+2.35	34.65+0.83
+ SCKD [107]	L2L	\times	\times	\times	72.33+1.55	72.10+3.00	34.76+0.94
+ CIRKD [68]	L2L	\times	\times	I	73.57 \ddagger +2.79	72.25+3.15	34.93+1.11
+ IFD [108]	L2L	\times	\times	\times	73.88 \ddagger +3.10	72.63+3.53	35.15 \ddagger +1.33
+ FGKD [82]	L2L	\times	\times	O	72.90 \ddagger +2.12	72.55+3.45	35.24+1.42
+ CWT [109]	L2L	\times	\times	O	73.06 \ddagger +2.28	72.60+3.50	35.21 \ddagger +1.39
+ SlimSeg [72]	L2L	\checkmark	E	\times	74.08+3.30	73.95+4.85	37.12+3.30
+ BGLSSeg [32]	L2L	\checkmark	E	\times	74.27 \ddagger +3.49	74.10 \ddagger +5.00	36.49 \ddagger +2.67
+ FAM [110]	L2L	\times	\times	\times	74.28 \ddagger +3.50	74.25+5.15	36.82 \ddagger +3.00
+ CrossKD [26]	L2L	\times	\times	\times	74.28 \ddagger +3.50	74.28+5.18	36.72 \ddagger +2.90
+ BPKD [73]	L2L	\checkmark	E	\times	74.30 \ddagger +3.52	74.29+5.19	37.07 \ddagger +3.25
+ BCKD _{ours}	W2W	\times	B	P	74.65+3.87	74.92+5.82	37.62+3.80
+ IFVD [20]	L2L	\times	\times	\times	74.05+3.27	74.41+5.31	36.63 \ddagger +3.35
+ IFVD + BCKD _{ours}	W2W	\times	B	P	74.82+4.04	74.99+5.89	37.73+3.91
+ TAT [111]	L2L	\times	\times	O	74.02 \ddagger +3.24	74.48+5.38	37.12+3.30
+ TAT + BCKD _{ours}	W2W	\times	B	P&O	74.71+3.93	74.97+5.87	38.12+4.30
+ SSTKD [83]	L2L	\checkmark	E	\times	73.91+3.13	74.60+5.50	37.22+3.40
+ SSTKD + BCKD _{ours}	W2W	\checkmark	B&E	P	74.52+3.74	74.90+5.80	38.24+4.52

3) *Visualized comparisons*: The visualized comparisons on the SSeg task with the baseline teacher and student models, and large models without the KD strategy are given in Figure 6. As highlighted by the white bounding boxes, the obtained results on Pascal VOC 2012 [28], Cityscapes [29], ADE20K [12], and COCO-Stuff 10K [30] demonstrate that BCKD yields significant improvements on both the boundary region completeness and the target region connectivity, when compared with the small student model’s results. For example, the “cow” in Pascal VOC 2012, the “guidepost” in Cityscapes, the “desk” and the “TV bench” in ADE20K, the “bus”, the “tennis racket”, and the “guideboard” in COCO-Stuff 10K. The results obtained are basically the same as those of the large teacher model. Besides, compared to large models with higher model complexity (*i.e.*, DANet [22] and HRNet [103]) on Pascal VOC 2012 and Cityscapes, although our method is not as competitive as theirs on quantitative results, our method achieves better predictions on object boundaries and small objects, which validate the effectiveness and emphasize the importance of boundary distillation and context distillation. With the help of our method, the student model is also able to predict better masks for certain fine-grained objects. For example, the “cow’s ear” and the “person’s leg”.

D. Comparisons With SOTA Methods on SSeg

In this section, we explore the superiority accuracy and the effectiveness of the joint implementation of BCKD with the state-of-the-art (SOTA) KD methods on SSeg. To ensure a fair comparison, PSPNet-101 [27] and DeepLabV3 Plus-101 [94] are employed as the teacher models, while PSPNet-18_(1.0) and

Table IV

COMPARISONS ON mIoU (%), MFS AND LHD WITH STATE-OF-THE-ART METHODS ON THE *test* SET OF COCO-STUFF 10K [30].

T: DeepLabV3 Plus-101		33.10%	1.00±0.00	0.00±0.00
S: DeepLabV3 Plus-18		26.33%	0.45±0.08	4.21±0.35
Methods	mIoU (%)	MFS (ρ_l)	LHD	
+ KD	27.21+0.88	0.63±0.07	3.82±0.41	
+ SKD	27.27+0.94	0.67±0.06	3.77±0.38	
+ SCKD	27.38+1.05	0.72±0.08	3.63±0.42	
+ CIRKD	27.68+1.35	0.81±0.05	3.45±0.33	
+ IFD	27.91+1.58	0.88±0.04	3.28±0.29	
+ FGKD	28.00+1.67	0.91±0.03	3.12±0.31	
+ CWT	28.18+1.85	0.95±0.02	2.98±0.22	
+ IFVD	28.35+2.02	1.02±0.03	2.77±0.25	
+ C2VKD	28.42+2.09	1.08±0.04	2.63±0.24	
+ FAM	28.48+2.15	1.12±0.03	2.55±0.21	
+ CrossKD	28.53+2.20	1.15±0.02	2.48±0.19	
+ SSTKD	28.70+2.37	1.23±0.03	2.31±0.17	
+ BCKD	29.22+2.89	1.41±0.02	1.89±0.15	
+ TAT	28.74+2.41	1.25±0.04	2.25±0.18	
+ TAT + BCKD	29.29+3.11	1.44±0.01	1.82±0.14	
+ SlimSeg	28.50+2.17	1.13±0.03	2.52±0.20	
+ SlimSeg + BCKD	29.45+3.12	1.46±0.01	1.79±0.13	
+ BPKD	28.66+2.33	1.21±0.02	2.36±0.16	
+ BPKD + BCKD	29.60+3.27	1.49±0.01	1.72±0.12	

DeepLabV3 Plus-18 [94] serve as the student models. The specific settings for each student model are described in detail in the provided table. Some results are re-implemented by us on the released code due to inconsistencies in experimental settings and are marked with “ \ddagger ” in the given tables.

1) *Superiority of BCKD*: Compared to the SOTA KD methods on SSeg, on the top half of Table III and Table IV, we can observe that our BCKD can surpass these methods. BCKD boosts the student model by 3.87%, 5.82%, and 3.80% mIoU \uparrow on the *val* sets of Pascal VOC 2012 [28], Cityscapes [29], and ADE20K [12], respectively. Compared to the current SOTA KD methods on these datasets, BCKD outperforms IFVD [20], TAT [111], and SSTKD [83] on Pascal VOC 2012 by 0.6%, 0.63%, and 0.74% mIoU \uparrow , respectively. The visualized comparison results with the classic KD [16] and SOTA IFVD methods are presented in the last row of Figure 5. It can be observed that our method demonstrates significant advantages in capturing the connectivity of small objects as well as the integrity of the boundary masks. Furthermore, BCKD achieves higher mIoU than SOTA methods on Cityscapes and ADE20K datasets as well. On the COCO-Stuff 10K [30] datasets in Table IV, our method surpasses the student model and the SOTA TAT model by 2.89% and 0.48% mIoU \uparrow , respectively. As demonstrated in Table IV, the proposed BCKD framework also exhibits significant advantages in terms of MFS (ρ_l) and LHD. These results not only indicate an overall performance improvement but also validate the effectiveness of our novel boundary distillation and context distillation, which were designed to address these critical aspects of the learning process. Since inference is only conducted on the student model, our method does not introduce any increase in model complexity. These results across different datasets can confirm that the task-specific knowledge is indeed more effective in practice compared to general knowledge.

2) *Effectiveness of the joint implementation*: The experimental results on the joint implementation of BCKD and SOTA KD methods are presented on the lower half of Table III and Table IV, respectively. It can be observed that, on top of BCKD, further adding IFVD [20], TAT [111], and SSTKD [83] yields consistent performance gains, with mIoU \uparrow improvements of 0.77%, 0.69%, and 0.61% on the *val* set of Pascal VOC 2012, respectively. This can be attributed to the fact that BCKD contains semantic boundary and context that is not present in these methods, further demonstrating the importance of semantic boundary and context information for the SSeg task. However, adding SSTKD [83] on top of BCKD resulted in a performance decrease (*i.e.*, 0.13% mIoU \downarrow on Pascal VOC 2012 and 0.02% mIoU \downarrow on Cityscapes) compared to the accuracy on BCKD. We guess that this may be because SSTKD uses superficial image texture information, which is non-semantic and contain some noise relative to the extracted semantic boundaries. On COCO-Stuff 10K, we can observe that our method further enhances the performance of all SOTA methods, including TAT [111], SlimSeg [72], and BPKD [73], and finally achieves 29.60% mIoU on the *test* set.

E. Comparisons With SOTA Methods on ISeg and ODet

The quantitative result comparisons on ISeg and ODet are presented in Table V. The obtained results indicate that our method can consistently outperform existing methods across various baseline models, demonstrating its strong generalization and versatility. Specifically, we achieve AP scores of

Table V
RESULT COMPARISONS WITH THE STATE-OF-THE-ART METHODS ON THE *val* SET OF MS-COCO 2017 [31] FOR ISEG AND ODET. “CM R-CNN”: CASCADE MASK R-CNN. MAP^m AND MAP^b DENOTES THE AVERAGE PRECISION ON INSTANCE SEGMENTATION MASK AND OBJECT DETECTION BOUNDING BOX, RESPECTIVELY.

Methods	AP ^m (%)	AP ^b (%)	FPS	MFS (ρ_l)	LHD
T: GFL-50 [99]	36.8	40.2	19.4	1.00	0.00
S: GFL-18 [99]	33.1	35.8	23.7	0.82	3.20
+ FGD [82]	34.0	36.6	23.7	0.85	2.90
+ SKD [76]	34.3	36.9	23.7	0.86	2.70
+ GID [112]	34.6	37.8	23.7	0.89	2.50
+ LD [69]	34.8	38.0	23.7	0.90	2.30
+ PKD [113]	35.0	38.0	23.7	0.91	2.20
+ CrossKD [26]	35.3	38.1	23.7	0.92	1.90
+ SSTKD [83]	35.2	38.3	23.7	0.93	1.80
+ BCKD _{ours}	35.8	38.8	23.7	0.95	1.60
T: CM R-CNN-101 [100]	37.3	42.9	13.1	1.00	0.00
S: CM R-CNN-50 [100]	36.5	41.9	16.1	0.88	2.10
+ FGD [82]	35.3	42.1	16.1	0.87	2.20
+ SKD [76]	36.5	42.2	16.1	0.89	2.00
+ GID [112]	36.7	42.0	16.1	0.90	1.90
+ LD [69]	36.8	42.1	16.1	0.91	1.80
+ PKD [113]	36.8	42.0	16.1	0.92	1.70
+ CrossKD [26]	36.9	42.2	16.1	0.93	1.60
+ SSTKD [83]	37.0	42.2	16.1	0.94	1.50
+ BCKD _{ours}	37.0	42.5	16.1	0.96	1.40
T: RetinaNet-101 [101]	33.5	38.9	13.5	1.00	0.00
S: RetinaNet-50 [101]	31.7	37.4	17.7	0.85	2.40
+ FGD [82]	32.1	37.7	17.7	0.86	2.20
+ SKD [76]	32.5	37.5	17.7	0.87	2.12
+ GID [112]	32.8	37.6	17.7	0.88	2.03
+ LD [69]	33.1	37.8	17.7	0.89	1.90
+ PKD [113]	33.0	37.8	17.7	0.90	1.88
+ CrossKD [26]	33.2	38.0	17.7	0.91	1.75
+ SSTKD [83]	33.1	38.1	17.7	0.92	1.66
+ BCKD _{ours}	33.3	38.5	17.7	0.94	1.54

35.8%/38.8%, 37.0%/42.5%, and 33.3%/38.5% for instance segmentation masks (*i.e.*, AP^m) and object detection bounding boxes (*i.e.*, AP^b) on the GFL-18 [99], Cascade Mask R-CNN-50 [100], and RetinaNet-50 [101], respectively. In comparison with the SOTA CrossKD [26] and SSTKD [83], our method demonstrates an average performance improvement of approximately 0.5%. This enhancement serves to validate the effectiveness of our proposed method. The results also demonstrate significant advantages in both MFS and LHD, indicating its superior capability in preserving the structure of learned feature manifolds while maintaining high precision in boundary-sensitive tasks. These results substantiate the effectiveness of our boundary and context distillation in maintaining geometric consistency and minimizing alignment errors.

The visual comparison results with baseline methods and SOTA methods are shown in Figure 7. It is observed that, relative to the baseline student models, the application of various KD strategies enhances the prediction results for specific classes (*e.g.*, the *person*”, the *book*”, and the *surfboard*”), thereby affirming the effectiveness of KD in dense image prediction tasks. Moreover, when compared to the SOTA methods CrossKD and SSTKD, our method demonstrates improved connectivity in object regions and boundary integrity (*e.g.*, the

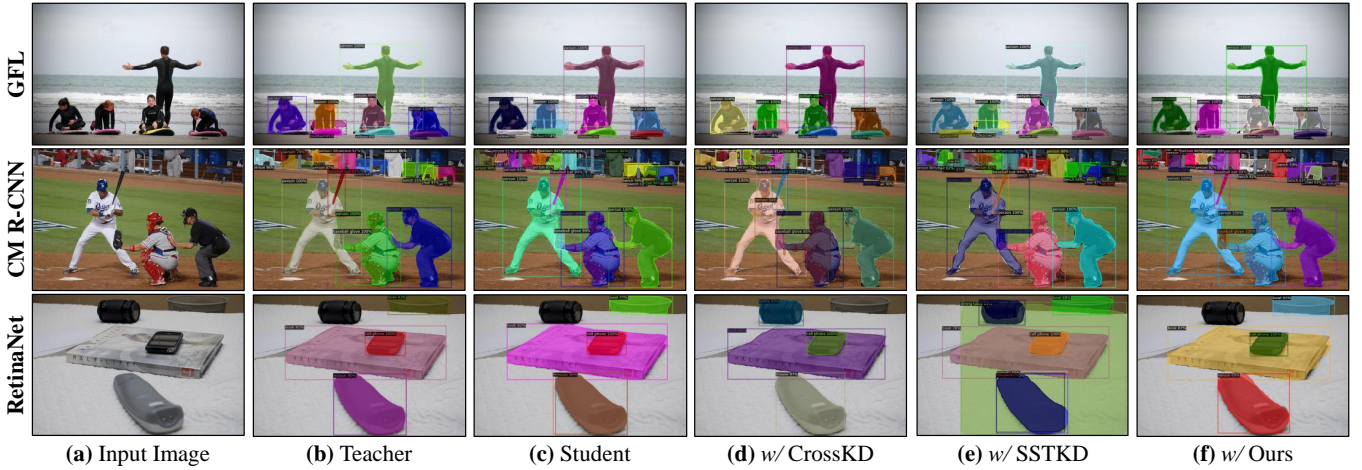


Figure 7. Visualization results on ISeg and ODet. “w/” means “with”, indicating that the corresponding knowledge distillation method is deployed based on the student model. We chose the state-of-the-art methods CrossKD [26] and SSTKD [83] for comparison.

person” and the *baseball bat*”), highlighting the effectiveness of our proposed context distillation and boundary distillation strategies tailored for the targeted tasks. Additionally, our method addresses the issue of overlapping predicted bounding boxes (e.g., the *mouse*” and the *chair*”), a benefit attributed to the enriched contextual information incorporated into the student model via context distillation.

Furthermore, we also observed a significant phenomenon wherein our method effectively reduces the occurrence of hallucinations in the student model’s predictions. Specifically, as depicted in the last column of Figure 7, both the teacher and student models fail to identify the *“camera”*, while the CrossKD and SSTKD methods mistakenly classify the *“camera”* as the *“bottle”*. In contrast, our approach accurately recognizes the *“camera”* as a background object, aligning with the dataset’s definitions. We hypothesize that this discrepancy may stem from the confusion of target knowledge caused by task-irrelevant KD during the training process. Our proposed task-specific BCKD is inherently designed to alleviate such confusion from the outset.

VI. CONCLUSION AND FUTURE WORK

In this work, we propose a customized boundary and context knowledge distillation (BCKD) method tailored for efficient dense image prediction tasks on AI accelerator, including semantic segmentation, instance segmentation, and object detection. Our approach significantly narrows the performance gap between compact, efficient models and their larger, more accurate counterparts while maintaining computational efficiency. Specifically, BCKD enhances boundary-region completeness and ensures object-region connectivity, leading to consistent accuracy improvements across diverse challenging benchmarks and architectures. Theoretical analysis further corroborates the effectiveness of our method.

As a generalizable method, in the future, we plan to extend BCKD to additional dense visual tasks (e.g., pose estimation and image synthesis) and investigate its adaptation to emerging architectures (e.g., Vision Transformer and Vision Mamba) to better support model compression for AI accelerator deployment. Moreover, we will explore synergies between BCKD

and large foundation models (e.g., Segment Anything Model and vision-language models) to further enhance the robustness of lightweight dense predictors under adverse conditions.

REFERENCES

- [1] J. Long, E. Shelhamer, and T. Darrell, “Fully convolutional networks for semantic segmentation,” in *The IEEE / CVF Computer Vision and Pattern Recognition Conference (CVPR)*, 2015, pp. 3431–3440.
- [2] R. Girshick, “Fast r-cnn,” in *Proceedings of the IEEE/CVF International Conference on Computer Vision (ICCV)*, 2015, pp. 1440–1448.
- [3] Y. Wang, Z. Xu, X. Wang, C. Shen, B. Cheng, H. Shen, and H. Xia, “End-to-end video instance segmentation with transformers,” in *The IEEE / CVF Computer Vision and Pattern Recognition Conference (CVPR)*, 2021, pp. 8741–8750.
- [4] D. Zhang, H. Zhang, J. Tang, X.-S. Hua, and Q. Sun, “Causal intervention for weakly-supervised semantic segmentation,” in *Advances in Neural Information Processing Systems (NeurIPS)*, 2020, pp. 655–666.
- [5] J. Ahn, S. Cho, and S. Kwak, “Weakly supervised learning of instance segmentation with inter-pixel relations,” in *The IEEE / CVF Computer Vision and Pattern Recognition Conference (CVPR)*, 2019, pp. 2209–2218.
- [6] H. Cao, Y. Wang, J. Chen, D. Jiang, X. Zhang, Q. Tian, and M. Wang, “Swin-unet: Unet-like pure transformer for medical image segmentation,” in *The European Conference on Computer Vision (ECCV)*, 2022, pp. 205–218.
- [7] R. Strudel, R. Garcia, I. Laptev, and C. Schmid, “Segmenter: Transformer for semantic segmentation,” in *Proceedings of the IEEE/CVF International Conference on Computer Vision (ICCV)*, 2021, pp. 7262–7272.
- [8] B. Cheng, I. Misra, A. G. Schwing, A. Kirillov, and R. Girdhar, “Masked-attention mask transformer for universal image segmentation,” in *The IEEE / CVF Computer Vision and Pattern Recognition Conference (CVPR)*, 2022, pp. 1290–1299.
- [9] M.-H. Guo, C.-Z. Lu, Q. Hou, Z. Liu, M.-M. Cheng, and S.-M. Hu, “Segnext: Rethinking convolutional attention design for semantic segmentation,” in *Advances in Neural Information Processing Systems (NeurIPS)*, 2022, pp. 1140–1156.
- [10] A. Kirillov, E. Mintun, N. Ravi, H. Mao, C. Rolland, L. Gustafson, T. Xiao, S. Whitehead, A. C. Berg, W.-Y. Lo *et al.*, “Segment anything,” in *Proceedings of the IEEE/CVF International Conference on Computer Vision (ICCV)*, 2023, pp. 4015–4026.
- [11] P. Dong, Y. Tan, X. Liu, P. Luo, Y. Liu, L. Liang, Y. Zhou, D. Pang, M.-T. Yung, D. Zhang *et al.*, “A 28nm 0.22 μ m/token memory-compute-intensity-aware cnn-transformer accelerator with hybrid-attention-based layer-fusion and cascaded pruning for semantic-segmentation,” in *IEEE International Solid-State Circuits Conference (ISSCC)*, vol. 68, 2025, pp. 01–03.
- [12] B. Zhou, H. Zhao, X. Puig, S. Fidler, A. Barriuso, and A. Torralba, “Scene parsing through ade20k dataset,” in *The IEEE / CVF Computer Vision and Pattern Recognition Conference (CVPR)*, 2017, pp. 633–641.

- [13] P. Dong, Z. Chen, Z. Li, Y. Fu, L. Chen, and F. An, "A 4.29 nj/pixel stereo depth coprocessor with pixel level pipeline and region optimized semi-global matching for iot application," *IEEE TCS*, vol. 69, no. 1, pp. 334–346, 2021.
- [14] D. Zhang, H. Zhang, J. Tang, X.-S. Hua, and Q. Sun, "Self-regulation for semantic segmentation," in *Proceedings of the IEEE/CVF International Conference on Computer Vision (ICCV)*, 2021, pp. 6953–6963.
- [15] D. Yin, Y. Yang, Z. Wang, H. Yu, K. Wei, and X. Sun, "1% vs 100%: Parameter-efficient low rank adapter for dense predictions," in *The IEEE / CVF Computer Vision and Pattern Recognition Conference (CVPR)*, 2023, pp. 20 116–20 126.
- [16] G. Hinton, O. Vinyals, and J. Dean, "Distilling the knowledge in a neural network," *arXiv*, 2015.
- [17] R. Wang, Y. Hao, L. Hu, X. Li, M. Chen, Y. Miao, and I. Humar, "Efficient crowd counting via dual knowledge distillation," *IEEE Transactions on Image Processing*, 2023.
- [18] B. Zhao, Q. Cui, R. Song, Y. Qiu, and J. Liang, "Decoupled knowledge distillation," in *The IEEE / CVF Computer Vision and Pattern Recognition Conference (CVPR)*, 2022, pp. 11 953–11 962.
- [19] K. Cui, Y. Yu, F. Zhan, S. Liao, S. Lu, and E. P. Xing, "Kd-dlgan: Data limited image generation via knowledge distillation," in *The IEEE / CVF Computer Vision and Pattern Recognition Conference (CVPR)*, 2023, pp. 3872–3882.
- [20] Y. Wang, W. Zhou, T. Jiang, X. Bai, and Y. Xu, "Intra-class feature variation distillation for semantic segmentation," in *The European Conference on Computer Vision (ECCV)*, 2020, pp. 346–362.
- [21] C. Wang, Y. Zhang, M. Cui, P. Ren, Y. Yang, X. Xie, X.-S. Hua, H. Bao, and W. Xu, "Active boundary loss for semantic segmentation," in *The Association for the Advancement of Artificial Intelligence (AAAI)*, 2022, pp. 2397–2405.
- [22] J. Fu, J. Liu, H. Tian, Y. Li, Y. Bao, Z. Fang, and H. Lu, "Dual attention network for scene segmentation," in *The IEEE / CVF Computer Vision and Pattern Recognition Conference (CVPR)*, 2019, pp. 3146–3154.
- [23] Y. Yuan, X. Chen, and J. Wang, "Object-contextual representations for semantic segmentation," in *The European Conference on Computer Vision (ECCV)*, 2020, pp. 173–190.
- [24] J. Gou, B. Yu, S. J. Maybank, and D. Tao, "Knowledge distillation: A survey," *International Journal of Computer Vision*, vol. 129, pp. 1789–1819, 2021.
- [25] K. Xu, L. Rui, Y. Li, and L. Gu, "Feature normalized knowledge distillation for image classification," in *The European Conference on Computer Vision (ECCV)*, 2020, pp. 664–680.
- [26] J. Wang, Y. Chen, Z. Zheng, X. Li, M.-M. Cheng, and Q. Hou, "Crosskd: Cross-head knowledge distillation for object detection," in *The IEEE / CVF Computer Vision and Pattern Recognition Conference (CVPR)*, 2024, pp. 16 520–16 530.
- [27] H. Zhao, J. Shi, X. Qi, X. Wang, and J. Jia, "Pyramid scene parsing network," in *The IEEE / CVF Computer Vision and Pattern Recognition Conference (CVPR)*, 2017, pp. 2881–2890.
- [28] M. Everingham, L. Van Gool, C. K. Williams, J. Winn, and A. Zisserman, "The pascal visual object classes (voc) challenge," *International Journal of Computer Vision*, vol. 88, pp. 303–338, 2010.
- [29] M. Cordts, M. Omran, S. Ramos, T. Rehfeld, M. Enzweiler, R. Benenson, U. Franke, S. Roth, and B. Schiele, "The cityscapes dataset for semantic urban scene understanding," in *The IEEE / CVF Computer Vision and Pattern Recognition Conference (CVPR)*, 2016, pp. 3213–3223.
- [30] H. Caesar, J. Uijlings, and V. Ferrari, "Coco-stuff: Thing and stuff classes in context," in *The IEEE / CVF Computer Vision and Pattern Recognition Conference (CVPR)*, 2018, pp. 1209–1218.
- [31] T.-Y. Lin, M. Maire, S. Belongie, J. Hays, P. Perona, D. Ramanan, P. Dollár, and C. L. Zitnick, "Microsoft coco: Common objects in context," in *The European Conference on Computer Vision (ECCV)*, 2014, pp. 740–755.
- [32] Q. Zhou, L. Wang, G. Gao, K. Bin, W. Ou, and H. Lu, "Boundary-guided lightweight semantic segmentation with multi-scale semantic context," *IEEE Transactions on Multimedia*, 2024.
- [33] J. Lin, Z. Xiao, X. Wei, P. Duan, X. He, R. Dian, Z. Li, and S. Li, "Click-pixel cognition fusion network with balanced cut for interactive image segmentation," *IEEE Transactions on Image Processing*, vol. 33, pp. 177–190, 2023.
- [34] C. Yu, J. Wang, C. Peng, C. Gao, G. Yu, and N. Sang, "Bisenet: Bilateral segmentation network for real-time semantic segmentation," in *The European Conference on Computer Vision (ECCV)*, 2018, pp. 325–341.
- [35] H. Noh, S. Hong, and B. Han, "Learning deconvolution network for semantic segmentation," in *Proceedings of the IEEE/CVF International Conference on Computer Vision (ICCV)*, 2015, pp. 1520–1528.
- [36] Z. Huang, X. Wang, L. Huang, C. Huang, Y. Wei, and W. Liu, "Ccnets: Criss-cross attention for semantic segmentation," in *The IEEE / CVF Computer Vision and Pattern Recognition Conference (CVPR)*, 2019, pp. 603–612.
- [37] A. Gu and T. Dao, "Mamba: Linear-time sequence modeling with selective state spaces," *arXiv*, 2023.
- [38] R. Xu, S. Yang, Y. Wang, B. Du, and H. Chen, "A survey on vision mamba: Models, applications and challenges," *arXiv*, 2024.
- [39] Z. Wang, X. Cun, J. Bao, W. Zhou, J. Liu, and H. Li, "Uformer: A general u-shaped transformer for image restoration," in *The IEEE / CVF Computer Vision and Pattern Recognition Conference (CVPR)*, 2022, pp. 17 683–17 693.
- [40] S. Zheng, J. Lu, H. Zhao, X. Zhu, Z. Luo, Y. Wang, Y. Fu, J. Feng, T. Xiang, P. H. Torr *et al.*, "Rethinking semantic segmentation from a sequence-to-sequence perspective with transformers," in *The IEEE / CVF Computer Vision and Pattern Recognition Conference (CVPR)*, 2021, pp. 6881–6890.
- [41] J. Li, X. Xia, W. Li, H. Li, X. Wang, X. Xiao, R. Wang, M. Zheng, and X. Pan, "Next-vit: Next generation vision transformer for efficient deployment in realistic industrial scenarios," *arXiv*, 2022.
- [42] Z. Peng, W. Huang, S. Gu, L. Xie, Y. Wang, J. Jiao, and Q. Ye, "Conformer: Local features coupling global representations for visual recognition," in *The IEEE / CVF Computer Vision and Pattern Recognition Conference (CVPR)*, 2021, pp. 367–376.
- [43] D. Zhang and K.-T. Cheng, "Generalized task-driven medical image quality enhancement with gradient promotion," *IEEE Transactions on Pattern Analysis and Machine Intelligence*, 2025.
- [44] H. Wu, B. Xiao, N. Codella, M. Liu, X. Dai, L. Yuan, and L. Zhang, "Cvt: Introducing convolutions to vision transformers," in *Proceedings of the IEEE/CVF International Conference on Computer Vision (ICCV)*, 2021, pp. 22–31.
- [45] D. Zhang, J. Tang, and K.-T. Cheng, "Graph reasoning transformer for image parsing," in *ACM International Conference on Multimedia (ACM MM)*, 2022, pp. 2380–2389.
- [46] D. Zhang, Y. Lin, J. Tang, and K.-T. Cheng, "Cae-great: Convolutional-auxiliary efficient graph reasoning transformer for dense image predictions," *International Journal of Computer Vision*, pp. 1–19, 2023.
- [47] E. Xie, W. Wang, Z. Yu, A. Anandkumar, J. M. Alvarez, and P. Luo, "Segformer: Simple and efficient design for semantic segmentation with transformers," in *Advances in Neural Information Processing Systems (NeurIPS)*, 2021, pp. 12 077–12 090.
- [48] J. Guo, K. Han, H. Wu, Y. Tang, X. Chen, Y. Wang, and C. Xu, "Cmt: Convolutional neural networks meet vision transformers," in *The IEEE / CVF Computer Vision and Pattern Recognition Conference (CVPR)*, 2022, pp. 12 175–12 185.
- [49] K. Han, Y. Wang, H. Chen, X. Chen, J. Guo, Z. Liu, Y. Tang, A. Xiao, C. Xu, Y. Xu *et al.*, "A survey on vision transformer," *IEEE Transactions on Pattern Analysis and Machine Intelligence*, vol. 45, no. 1, pp. 87–110, 2022.
- [50] X. Mao, G. Qi, Y. Chen, X. Li, R. Duan, S. Ye, Y. He, and H. Xue, "Towards robust vision transformer," in *The IEEE / CVF Computer Vision and Pattern Recognition Conference (CVPR)*, 2022, pp. 12 042–12 051.
- [51] W. Wang, E. Xie, X. Li, D.-P. Fan, K. Song, D. Liang, T. Lu, P. Luo, and L. Shao, "Pyramid vision transformer: A versatile backbone for dense prediction without convolutions," in *Proceedings of the IEEE/CVF International Conference on Computer Vision (ICCV)*, 2021, pp. 568–578.
- [52] Z. Kong, P. Dong, X. Ma, X. Meng, W. Niu, M. Sun, X. Shen, G. Yuan, B. Ren, H. Tang *et al.*, "Svpt: Enabling faster vision transformers via latency-aware soft token pruning," in *The European Conference on Computer Vision (ECCV)*, 2022, pp. 620–640.
- [53] H. Fan, B. Xiong, K. Mangalam, Y. Li, Z. Yan, J. Malik, and C. Feichtenhofer, "Multiscale vision transformers," in *Proceedings of the IEEE/CVF International Conference on Computer Vision (ICCV)*, 2021, pp. 6824–6835.
- [54] P. Dong, Z. Chen, K. Li, L. Chen, K.-T. Cheng, and F. An, "A 1920×1080 129fps 4.3 pj/pixel stereo-matching processor for pico aerial vehicles," in *ESSCIRC*, 2023, pp. 345–348.
- [55] W. Chen, Y. Huang, M. Wang, X. Wu, and X. Zeng, "Kbstyle: Fast style transfer using a 200 kb network with symmetric knowledge distillation," *IEEE Transactions on Image Processing*, vol. 33, pp. 82–94, 2023.

- [56] J. Gou, X. Xiong, B. Yu, L. Du, Y. Zhan, and D. Tao, "Multi-target knowledge distillation via student self-reflection," *International Journal of Computer Vision*, pp. 1–18, 2023.
- [57] W.-C. Tseng, T.-H. J. Wang, Y.-C. Lin, and P. Isola, "Offline multi-agent reinforcement learning with knowledge distillation," in *Advances in Neural Information Processing Systems (NeurIPS)*, 2022, pp. 226–237.
- [58] Q. Guo, X. Wang, Y. Wu, Z. Yu, D. Liang, X. Hu, and P. Luo, "Online knowledge distillation via collaborative learning," in *The IEEE / CVF Computer Vision and Pattern Recognition Conference (CVPR)*, 2020, pp. 11 020–11 029.
- [59] L. Zhang, J. Song, A. Gao, J. Chen, C. Bao, and K. Ma, "Be your own teacher: Improve the performance of convolutional neural networks via self distillation," in *Proceedings of the IEEE/CVF International Conference on Computer Vision (ICCV)*, 2019, pp. 3713–3722.
- [60] F. Yuan, L. Shou, J. Pei, W. Lin, M. Gong, Y. Fu, and D. Jiang, "Reinforced multi-teacher selection for knowledge distillation," in *The Association for the Advancement of Artificial Intelligence (AAAI)*, 2021, pp. 14 284–14 291.
- [61] P. Passban, Y. Wu, M. Rezagholizadeh, and Q. Liu, "Alp-kd: Attention-based layer projection for knowledge distillation," in *The Association for the Advancement of Artificial Intelligence (AAAI)*, 2021, pp. 13 657–13 665.
- [62] S. Lee and B. C. Song, "Graph-based knowledge distillation by multi-head attention network," *arXiv*, 2019.
- [63] R. Sun, F. Tang, X. Zhang, H. Xiong, and Q. Tian, "Distilling object detectors with task adaptive regularization," *arXiv*, 2020.
- [64] G. Chen, W. Choi, X. Yu, T. Han, and M. Chandraker, "Learning efficient object detection models with knowledge distillation," in *Advances in Neural Information Processing Systems (NeurIPS)*, 2017.
- [65] T. Wang, L. Yuan, X. Zhang, and J. Feng, "Distilling object detectors with fine-grained feature imitation," in *The IEEE / CVF Computer Vision and Pattern Recognition Conference (CVPR)*, 2019, pp. 4933–4942.
- [66] D. Zhang, C. Zuo, Q. Wu, L. Fu, and X. Xiang, "Unabridged adjacent modulation for clothing parsing," *Pattern Recognition*, vol. 127, p. 108594, 2022.
- [67] H. Zhang, K. Dana, J. Shi, Z. Zhang, X. Wang, A. Tyagi, and A. Agrawal, "Context encoding for semantic segmentation," in *The IEEE / CVF Computer Vision and Pattern Recognition Conference (CVPR)*, 2018, pp. 7151–7160.
- [68] C. Yang, H. Zhou, Z. An, X. Jiang, Y. Xu, and Q. Zhang, "Cross-image relational knowledge distillation for semantic segmentation," in *The IEEE / CVF Computer Vision and Pattern Recognition Conference (CVPR)*, 2022, pp. 12 319–12 328.
- [69] Z. Zheng, R. Ye, P. Wang, D. Ren, W. Zuo, Q. Hou, and M.-M. Cheng, "Localization distillation for dense object detection," in *The IEEE / CVF Computer Vision and Pattern Recognition Conference (CVPR)*, 2022.
- [70] D. Zhixing, R. Zhang, M. Chang, S. Liu, T. Chen, Y. Chen *et al.*, "Distilling object detectors with feature richness," in *Advances in Neural Information Processing Systems (NeurIPS)*, 2021, pp. 5213–5224.
- [71] Y. Lin, D. Zhang, X. Fang, Y. Chen, K.-T. Cheng, and H. Chen, "Rethinking boundary detection in deep learning models for medical image segmentation," in *Information Processing In Medical Imaging*, 2023, pp. 730–742.
- [72] D. Xue, F. Yang, P. Wang, L. Herranz, J. Sun, Y. Zhu, and Y. Zhang, "Slimseg: Slimmable semantic segmentation with boundary supervision," in *ACM International Conference on Multimedia (ACM MM)*, 2022, pp. 6539–6548.
- [73] L. Liu, Z. Wang, M. H. Phan, B. Zhang, J. Ge, and Y. Liu, "Bpkd: Boundary privileged knowledge distillation for semantic segmentation," in *IEEE/CVF Winter Conference on Applications of Computer Vision (WACV)*, 2024, pp. 1062–1072.
- [74] M. Ji, S. Shin, S. Hwang, G. Park, and I.-C. Moon, "Refine myself by teaching myself: Feature refinement via self-knowledge distillation," in *The IEEE / CVF Computer Vision and Pattern Recognition Conference (CVPR)*, 2021, pp. 10 664–10 673.
- [75] M. Phuong and C. H. Lampert, "Distillation-based training for multi-exit architectures," in *Proceedings of the IEEE/CVF International Conference on Computer Vision (ICCV)*, 2019, pp. 1355–1364.
- [76] Y. Liu, K. Chen, C. Liu, Z. Qin, Z. Luo, and J. Wang, "Structured knowledge distillation for semantic segmentation," in *The IEEE / CVF Computer Vision and Pattern Recognition Conference (CVPR)*, 2019, pp. 2604–2613.
- [77] R. Liu, K. Yang, A. Roitberg, J. Zhang, K. Peng, H. Liu, and R. Stiefelham, "Transkd: Transformer knowledge distillation for efficient semantic segmentation," *arXiv*, 2022.
- [78] X. Zheng, Y. Luo, P. Zhou, and L. Wang, "Distilling efficient vision transformers from cnns for semantic segmentation," *arXiv*, 2023.
- [79] J. Ahn and S. Kwak, "Learning pixel-level semantic affinity with image-level supervision for weakly supervised semantic segmentation," in *The IEEE / CVF Computer Vision and Pattern Recognition Conference (CVPR)*, 2018, pp. 4981–4990.
- [80] L. Chen, W. Wu, C. Fu, X. Han, and Y. Zhang, "Weakly supervised semantic segmentation with boundary exploration," in *The European Conference on Computer Vision (ECCV)*, 2020, pp. 347–362.
- [81] L. Ru, Y. Zhan, B. Yu, and B. Du, "Learning affinity from attention: End-to-end weakly-supervised semantic segmentation with transformers," in *The IEEE / CVF Computer Vision and Pattern Recognition Conference (CVPR)*, 2022, pp. 16 846–16 855.
- [82] Z. Yang, Z. Li, X. Jiang, Y. Gong, Z. Yuan, D. Zhao, and C. Yuan, "Focal and global knowledge distillation for detectors," in *The IEEE / CVF Computer Vision and Pattern Recognition Conference (CVPR)*, 2022, pp. 4643–4652.
- [83] D. Ji, H. Wang, M. Tao, J. Huang, X.-S. Hua, and H. Lu, "Structural and statistical texture knowledge distillation for semantic segmentation," in *The IEEE / CVF Computer Vision and Pattern Recognition Conference (CVPR)*, 2022, pp. 16 876–16 885.
- [84] M. Caron, H. Touvron, I. Misra, H. Jégou, J. Mairal, P. Bojanowski, and A. Joulin, "Emerging properties in self-supervised vision transformers," in *Proceedings of the IEEE/CVF International Conference on Computer Vision (ICCV)*, 2021, pp. 9650–9660.
- [85] X. Wang, R. Zhang, C. Shen, T. Kong, and L. Li, "Dense contrastive learning for self-supervised visual pre-training," in *The IEEE / CVF Computer Vision and Pattern Recognition Conference (CVPR)*, 2021, pp. 3024–3033.
- [86] Z.-Y. Li, S. Gao, and M.-M. Cheng, "Exploring feature self-relation for self-supervised transformer," *arXiv*, 2022.
- [87] F. Lin, Z. Liang, S. Wu, J. He, K. Chen, and S. Tian, "Structtoken: Rethinking semantic segmentation with structural prior," *IEEE Transactions on Circuits and Systems for Video Technology*, 2023.
- [88] W. Xie, Z. Zhao, S. Li, B. Zuo, and Y. Wang, "Nonrigid object contact estimation with regional unwrapping transformer," in *Proceedings of the IEEE/CVF International Conference on Computer Vision (ICCV)*, 2023, pp. 9342–9351.
- [89] Z. Yang, A. Zeng, C. Yuan, and Y. Li, "Effective whole-body pose estimation with two-stages distillation," in *Proceedings of the IEEE/CVF International Conference on Computer Vision (ICCV)*, 2023, pp. 4210–4220.
- [90] R. Kanwal and K. Liu, "A taylor expansion approach for solving integral equations," *International Journal of Mathematical Education in Science and Technology*, vol. 20, no. 3, pp. 411–414, 1989.
- [91] K. J. Falconer and J. D. Howroyd, "Projection theorems for box and packing dimensions," in *Mathematical Proceedings of the Cambridge Philosophical Society*, vol. 119, no. 2. Cambridge University Press, 1996, pp. 287–295.
- [92] T. L. Lai, "Stochastic approximation," *The annals of Statistics*, vol. 31, no. 2, pp. 391–406, 2003.
- [93] A. Paszke, S. Gross, F. Massa, A. Lerer, J. Bradbury, G. Chanan, T. Killeen, Z. Lin, N. Gimelshein, L. Antiga *et al.*, "Pytorch: An imperative style, high-performance deep learning library," in *Advances in Neural Information Processing Systems (NeurIPS)*, 2019.
- [94] L.-C. Chen, Y. Zhu, G. Papandreou, F. Schroff, and H. Adam, "Encoder-decoder with atrous separable convolution for semantic image segmentation," in *The European Conference on Computer Vision (ECCV)*, 2018, pp. 801–818.
- [95] K. He, X. Zhang, S. Ren, and J. Sun, "Deep residual learning for image recognition," in *The IEEE / CVF Computer Vision and Pattern Recognition Conference (CVPR)*, 2016, pp. 770–778.
- [96] H. Liu, "Lightnet: Light-weight networks for semantic image segmentation," *LighCNeC. html*, vol. 5, p. 6, 2018.
- [97] M. Tan and Q. Le, "Efficientnet: Rethinking model scaling for convolutional neural networks," in *The International Conference on Machine Learning (ICML)*, 2019, pp. 6105–6114.
- [98] L. Zhang and K. Ma, "Structured knowledge distillation for accurate and efficient object detection," *IEEE Transactions on Pattern Analysis and Machine Intelligence*, 2023.
- [99] X. Li, W. Wang, L. Wu, S. Chen, X. Hu, J. Li, J. Tang, and J. Yang, "Generalized focal loss: Learning qualified and distributed bounding boxes for dense object detection," in *Advances in Neural Information Processing Systems (NeurIPS)*, 2020, pp. 21 002–21 012.

- [100] Z. Cai and N. Vasconcelos, "Cascade r-cnn: Delving into high quality object detection," in *The IEEE / CVF Computer Vision and Pattern Recognition Conference (CVPR)*, 2018, pp. 6154–6162.
- [101] T.-Y. Ross and G. Dollár, "Focal loss for dense object detection," in *The IEEE / CVF Computer Vision and Pattern Recognition Conference (CVPR)*, 2017, pp. 2980–2988.
- [102] J. Deng, W. Dong, R. Socher, L.-J. Li, K. Li, and L. Fei-Fei, "Imagenet: A large-scale hierarchical image database," in *The IEEE / CVF Computer Vision and Pattern Recognition Conference (CVPR)*, 2009, pp. 248–255.
- [103] K. Sun, Y. Zhao, B. Jiang, T. Cheng, B. Xiao, D. Liu, Y. Mu, X. Wang, W. Liu, and J. Wang, "High-resolution representations for labeling pixels and regions," *arXiv*, 2019.
- [104] L.-C. Chen, G. Papandreou, I. Kokkinos, K. Murphy, and A. L. Yuille, "Deeplab: Semantic image segmentation with deep convolutional nets, atrous convolution, and fully connected crfs," *IEEE Transactions on Pattern Analysis and Machine Intelligence*, vol. 40, no. 4, pp. 834–848, 2017.
- [105] S. Mehta, M. Rastegari, A. Caspi, L. Shapiro, and H. Hajishirzi, "Espnet: Efficient spatial pyramid of dilated convolutions for semantic segmentation," in *The European Conference on Computer Vision (ECCV)*, 2018, pp. 552–568.
- [106] B. Zhang, Z. Tian, Q. Tang, X. Chu, X. Wei, C. Shen *et al.*, "Segvit: Semantic segmentation with plain vision transformers," in *Advances in Neural Information Processing Systems (NeurIPS)*, 2022, pp. 4971–4982.
- [107] Y. Zhu and Y. Wang, "Student customized knowledge distillation: Bridging the gap between student and teacher," in *Proceedings of the IEEE/CVF International Conference on Computer Vision (ICCV)*, 2021, pp. 5057–5066.
- [108] Y. Chen, S. Wang, J. Liu, X. Xu, F. de Hoog, and Z. Huang, "Improved feature distillation via projector ensemble," in *Advances in Neural Information Processing Systems (NeurIPS)*, 2022, pp. 12 084–12 095.
- [109] Z. Liu, Y. Wang, X. Chu, N. Dong, S. Qi, and H. Ling, "A simple and generic framework for feature distillation via channel-wise transformation," in *Proceedings of the IEEE/CVF International Conference on Computer Vision (ICCV) Workshops*, 2023, pp. 1129–1138.
- [110] C. Pham, V.-A. Nguyen, T. Le, D. Phung, G. Carneiro, and T.-T. Do, "Frequency attention for knowledge distillation," in *IEEE/CVF Winter Conference on Applications of Computer Vision (WACV)*, 2024, pp. 2277–2286.
- [111] S. Lin, H. Xie, B. Wang, K. Yu, X. Chang, X. Liang, and G. Wang, "Knowledge distillation via the target-aware transformer," in *The IEEE / CVF Computer Vision and Pattern Recognition Conference (CVPR)*, 2022, pp. 10 915–10 924.
- [112] X. Dai, Z. Jiang, Z. Wu, Y. Bao, Z. Wang, S. Liu, and E. Zhou, "General instance distillation for object detection," in *The IEEE / CVF Computer Vision and Pattern Recognition Conference (CVPR)*, 2021, pp. 7842–7851.
- [113] W. Cao, Y. Zhang, J. Gao, A. Cheng, K. Cheng, and J. Cheng, "Pkd: General distillation framework for object detectors via pearson correlation coefficient," in *Advances in Neural Information Processing Systems (NeurIPS)*, 2022, pp. 15 394–15 406.